

RAINER PÄRNA

Surface studies
of some oxide films



TARTU UNIVERSITY PRESS

Institute of Physics, Faculty of Science and Technology, University of Tartu, Estonia

Dissertation in Materials Science

The Dissertation was admitted on November 23, 2011, in partial fulfilment of the requirements for the degree of Doctor of Philosophy in materials science, and allowed for defence by the Scientific Council on Materials Science of the Faculty of Science and Technology of the University of Tartu.

Supervisors: Dr. Vambola Kisand, Institute of Physics, University of Tartu
Prof. Ergo Nõmmiste, Institute of Physics, University of Tartu

Opponent: Prof. Nils Mårtensson, Department of Physics and Astronomy, Uppsala University

Commencement: January 27, 2012 at University of Tartu, Tartu, Estonia

“This work has been supported by graduate school „Functional materials and technologies“ receiving funding from the European Social Fund under project 1.2.0401.09-0079 in Estonia.”



European Union
European Social Fund



Investing in your future

ISSN 2228–0928

ISBN 978–9949–19–920–4 (trükis)

ISBN 978–9949–19–921–1 (PDF)

Autoriõigus: Rainer Pärna, 2011

Tartu Ülikooli Kirjastus

www.tyk.ee

Tellimus nr. 805

TABLE OF CONTENTS

LIST OF PUBLICATIONS	7
AUTHOR'S CONTRIBUTION	8
ABBREVIATIONS AND SYMBOLS	9
1. INTRODUCTION	10
2. MOTIVATION AND AIM OF THE WORK	13
3. OVERVIEW OF TITANIA AND STAINLESS STEEL	14
3.1. Titania	14
3.1.1. General remarks about titania	14
3.1.2. Photocatalysis	18
3.1.3. Light-induced hydrophilicity	19
3.2. Stainless steel	21
4. THIN FILM PREPARATION	24
4.1. Sol-gel method	24
4.1.1. Preparation of undoped, cobalt- and nickel-containing titania films	24
4.2. TiC-enriched austenitic stainless steel preparation and surface oxidation	26
5. X-RAY ABSORPTION	27
5.1. X-ray absorption spectroscopy	27
5.2. X-ray photoelectron spectroscopy	31
6. EXPERIMENTAL	33
6.1. Synchrotron radiation	33
6.2. XPS and XAS measurement systems	34
6.2.1. Beamline D1011	34
6.2.2. Beamline I511	34
6.2.3. Surface station at Institute of Physics University of Tartu	35
6.3. XPS and XAS experimental details	35
6.3.1. Undoped, cobalt- and nickel-containing titania	35
6.3.2. TiC-enriched stainless steel	36
6.4. X-ray diffraction	36
6.4.1. Experimental details of x-ray diffraction	37
6.5. Other film characterization techniques	38
7. RESULTS AND DISCUSSION	40
7.1. Effect of cobalt and nickel addition to titania (Papers II–IV)	40
7.2. XPS and XAS study of stainless steel surface oxidation (Paper I) ...	56

SUMMARY	63
SUMMARY IN ESTONIAN	66
ACKNOWLEDGEMENT	69
REFERENCES	70
PUBLICATIONS	75

LIST OF PUBLICATIONS

- I. **R. Pärna**, E. Nõmmiste, A. Kikas, P. Jussila, M. Hirsimäki, M. Valden, V. Kisand, “Electron spectroscopic study of passive oxide layer formation on Fe–19Cr–18Ni–1Al–TiC austenitic stainless steel”, *Journal of Electron Spectroscopy and Related Phenomena* 182 (2010) 108–114.
- II. V. Kisand, U. Joost, V. Reedo, **R. Pärna**, T. Tätte, J. Shulga, A. Saar, L. Matisen, A. Kikas, I. Kink, “Influence of the heating temperature on the properties of nickel doped TiO₂ films prepared by sol-gel method”, *Applied Surface Science* 256 (2010) 4538–4542.
- III. **R. Pärna**, U. Joost, E. Nõmmiste, T. Käämbre, A. Kikas, I. Kuusik, M. Hirsimäki, I. Kink, V. Kisand, “Effect of cobalt doping and annealing on properties of titania thin films prepared by sol-gel process”, *Applied Surface Science* 257 (2011) 6897–6907.
- IV. **R. Pärna**, U. Joost, E. Nõmmiste, T. Käämbre, A. Kikas, I. Kuusik, M. Hirsimäki, I. Kink, V. Kisand, “Effect of different annealing temperatures and SiO₂/Si(100) substrate on the properties of nickel containing titania thin sol-gel films”, *Physica Status Solidi A* (submitted).

OTHER RELATED PUBLICATIONS THAT ARE NOT INCLUDED IN THE THESIS

- V. **R. Pärna**, A. Tarre, A. Gerst, H. Mändar, A. Niilisk, T. Uustare, A. Rosental, V. Sammelselg, “Influence of annealing on atomic layer deposited TiO₂–Cr₂O₃ thin films”, *Proceedings of SPIE* 6596 (2007) 59618–59618.
- VI. A. Tarre, J. Aarik, H. Mändar, A. Niilisk, **R. Pärna**, R. Rammula, T. Uustare, A. Rosental, V. Sammelselg, “Atomic layer deposition of Cr₂O₃ thin films: Effect of crystallization on growth and properties”, *Applied Surface Science* 254 (2008) 5149–5156.
- VII. V. Sammelselg, A. Tarre, J. Lu, J. Aarik, A. Niilisk, T. Uustare, I. Netšipailo, R. Rammula, **R. Pärna**, A. Rosental, “Structural characterization of TiO₂–Cr₂O₃ nanolaminates grown by atomic layer deposition”, *Surface & Coatings Technology* 204 (2010) 2015–2018.
- VIII. L. Kanninen, N. Jokinen, H. Ali-Löytty, P. Jussila, K. Lahtonen, M. Hirsimäki, M. Valden, M. Kuzmin, **R. Pärna**, E. Nõmmiste, “Adsorption structure and bonding of trimesic acid on Cu(100)”, *Surface Science* 605 (2011) 1968–1978.

AUTHOR'S CONTRIBUTION

As can be seen from the list of publications the research involves an output of numerous people. The reason lies in the complex nature of the samples, that requires the applying of various experimental techniques for their characterization and an expertise of a number of scientists. The outcome produced within the frame of the research papers is a group effort.

The Author's contribution to each research paper is given in the list below. Roman numbers correspond to the numbers in list of publications.

- I. The Author is responsible for the manuscript and figures. He analysed XPS and XAS data.
- II. The Author participated in the preparation of the manuscript. He conducted XRD measurements and analysed XRD data.
- III. The Author is responsible for the manuscript and figures. He participated in XPS and XAS measurements, analysed XPS and XAS data. He carried out the majority of XRD and XRR measurements, analysed XRD data, interpreted the Raman spectra, analysed AFM images, participated in SEM and EDX measurements.
- IV. The Author is responsible for the manuscript and figures. He participated in XPS and XAS measurements, analysed XPS and XAS data. He carried out the majority of XRD and XRR measurements, analysed XRD data, interpreted the Raman spectra, analysed AFM images, and carried out supplementary hydrophilicity measurements.

ABBREVIATIONS AND SYMBOLS

AFM	atomic force microscopy
bcc	body-centered cubic lattice
CB	conduction band
CCD	charged couple device
DOS	density of states
EDX	energy dispersive x-ray analysis
EXAFS	extended x-ray absorption fine structure
FAT	fixed analyser transmission
fcc	face-centered cubic lattice
FIB – SEM	focused ion beam – scanning electron microscope
MCP	microchannel plate
NEXAFS	near edge x-ray absorption fine structure
PEY	partial electron yield
RMS	root mean square
SEM	scanning electron microscopy
TEY	total electron yield
UHV	ultra-high vacuum
UV-Vis	ultraviolet-visible spectroscopy
VB	valence band
XANES	x-ray absorption near edge spectroscopy
XAS	x-ray absorption spectroscopy
XES	x-ray emission spectroscopy
XPS	x-ray photoelectron spectroscopy
XRD	x-ray diffraction
XRR	x-ray reflection
A_{ads}	adsorbed acceptor
D_{ads}	adsorbed donor
e^-	electron
E_b	binding energy
E_g	band gap
E_k	kinetic energy
eV	electron volt
h^+	hole (electronic vacancy)
HF	hydrofluoric acid
H_2O_2	hydrogen peroxide
h ν	photon energy
O_2	oxygen
OH^-	hydroxyl group
Φ	work function
$\bullet HO_2$	hydroperoxide radical
$\bullet OH$	hydroxyl radical
$\bullet O_2^-$	superoxide ion

I. INTRODUCTION

Titanium(IV) oxide (TiO_2 , titania) and chromium(III) oxide (Cr_2O_3 , chromia) attract great attention for numerous advanced applications. Many research groups investigate TiO_2 as a photocatalyst [1], a solar cell material [2], a material for anti-fogging coating and self-cleaning coating [3,4] and a sensor material [5]. If titania's photocatalytic and light-induced hydrophilic characteristics (anti-fogging property) are combined, self-cleaning windows can be prepared. Cr_2O_3 has potential applications in catalysis [6], sensorics [7], solar cells [8] and wear protective coatings [9]. Furthermore, a thin chromium-rich oxide film on the surface of stainless steel is responsible for the alloy's durability to rust [10]. Stainless steel has applications in a number of fields, for example, in tableware, food industry, medicine, chemistry, automotive technology, etc. In addition, custom grade stainless steels with modified composition are prepared for specific applications.

Pure titania in the applications using sunlight has some drawbacks, which limit its usage. In the applications where sunlight is collected, an effective electron-hole pair generation and a long lifetime of electron-hole pairs are required. Unfortunately, titania absorbs only a fraction of sunlight. Its band gap depends on the crystal structure and is typically 3.2 eV in case of anatase and 3.0 eV in case of rutile [11]. Therefore, it would be technologically and economically advantageous to enhance titania absorption of sunlight.

Under ambient conditions spontaneously formed chromium-rich oxide film (i.e. protective oxide layer) on the surface of stainless steel is responsible for the alloy's good corrosion resistance in oxidizing environments. Nevertheless, in some specific applications, a more enhanced passive oxide film on the surface of stainless steel is needed, for example, in nuclear applications [12, 13].

Several difficulties can be overcome by introducing additives to the structure of materials (doping). Impurities modify the electronic structure of material, which can enhance its physical and chemical properties. Previously it has been reported, that cobalt and nickel addition to titania has improved its catalytic properties and the absorption edge has shifted towards the visible light maximum of solar radiation [14–16]. It has been demonstrated that the corrosion resistance of stainless steel has been improved by adding such elements as Si, N, Ti or Nb [12, 13, 17].

To introduce impurity into the virgin material, different methods are used. For practical applications the sol-gel deposition has become widely used because of the numerous advantages it has over other fabrication techniques. In certain cases important aspects of film preparation, such as flexibility in introducing impurity in large concentrations, homogeneity, stoichiometry, ability to coat large and complex surfaces, and cost-effectiveness, can be enhanced by using the sol-gel deposition [11]. However, to obtain the crystal structure of films after sol-gel deposition, annealing has to be carried out.

Additives are introduced to steel materials in the process of material preparation. To achieve certain compound segregation thermal treatment is carried out.

Whenever impurities are introduced to a pure material, a possibility of some element or compound segregation to the surface or the bulk arises. Special attention should be paid to these processes when doped materials are annealed. The most common method of determining the formation of material crystallite phases is x-ray diffraction (XRD). Besides XRD the Raman spectroscopy can also provide information concerning crystal phases. To enhance knowledge about additives distribution in material, x-ray fluorescence mapping of certain elements could be beneficial [Papers III–IV].

Cobalt addition to titania has received attention in literature [14, 18, 19]. Less attention has been paid to nickel incorporation to titania [16]. In the case of each specific stainless steel, additives segregation to grain boundary, surface, bulk or interface region should be studied in order to understand the additives effect on alloy properties and corrosion resistance.

To gain better knowledge about the elements and compounds in the surface region of pristine titania, doped titania and stainless steel, surface-sensitive methods have to be applied. A common technique for obtaining information about the electronic structure and the chemical state of a solid surface is x-ray photoelectron spectroscopy (XPS). XPS is based on a photoelectric effect, where absorbed photons liberate photoelectrons, which are analysed with respect to their kinetic energy. XPS is a surface-sensitive method thanks to a small electron mean free path of the excited-electrons in solids, which is typically in the range of 5–20 Å [20]. Besides XPS, x-ray absorption spectroscopy (XAS) is also a surface-sensitive method. XAS is known as a highly versatile tool for determining the local electronic structure and the chemical state of matter. This method is based on a local nature of x-ray absorption process, where an electron is excited from a core state to an unoccupied state. In a total electron yield (TEY) mode, the absorption cross section is measured by detecting and counting electrons with all kinds of kinetic energies, which escape from the surface after the decay of the core hole. XAS in TEY mode has the probing depth of 50 Å and a deeper for transition metal 2p edges [21]. To carry out XPS and XAS experiments ultra-high vacuum (UHV) conditions are needed.

The surface and bulk properties of sol-gel deposited undoped and doped titania powders and thick films (much more than 100 nm thick) have been extensively studied. However, it is clear that the film thickness has influence on its properties. Therefore, more knowledge is needed about the properties of titania thin films and it is necessary to study the effects of additives and annealing temperature upon the properties of these systems. In addition, little attention has been paid in literature to the effect of Si substrate upon the properties of thin sol-gel deposited films. Since the chemical and physical properties of the substrate surface can influence the deposited film structure [22], studies of the films prepared comparably on SiO₂/Si(100) (i.e. with native oxide layer) and on HF-etched Si(100) (i.e. without native oxide layer) are needed.

A passive chromium-rich oxide film (i.e. protective oxide layer) is spontaneously formed on the surface of stainless steel. It is typically 1–3 nm thick and it protects the alloy from further oxidation. To achieve a better understanding of the passive oxide layer formation and the dependence of its properties on the additives, detailed studies with surface-sensitive methods in well-defined experimental conditions are needed. One possibility is to carry out measurements *in situ* in UHV conditions by using XPS and XAS. Predominantly the surface analytical studies of the oxidation of stainless steel materials have been made *ex situ*, there are only a few exceptions, where the onset of the oxidation process of stainless steel alloys has been studied *in situ* [23, 24].

Although the impurity addition to titania films and the formation of a thin chromium-rich oxide film on the surface of stainless steel with additives are in focus of many research groups and the number of publications in these fields is growing every year, a number of questions remain unsolved and need to be studied. In particular, the segregation of additives in films, the influence of films thickness and the effect of substrates on the properties of films are not fully understood yet. In order to gain better knowledge about the formation of a protective chromium-rich oxide layer on the surface of stainless steel, alloy oxidation studies in a controlled environment by using defined oxygen exposures are needed.

In order to give the reader a better overview, the thesis is built up as follows: in Chapter 2 motivation and aim of the work is defined, Chapter 3 gives an overview of the materials studied in Papers I-IV; Chapter 4 gives an overview of the materials preparation techniques used in Papers I-IV; in Chapter 5 the principles of XAS and XPS are described; Chapter 6 is focused on the characterization of the techniques mostly used in the papers included; Chapter 7 is dedicated to the experimental results and discussion.

2. MOTIVATION AND AIM OF THE WORK

Titania is a material that has several important properties. It is a well-known photocatalyst and its surface has a light-induced super-hydrophilic property. This enables, besides other applications, the preparation of self-cleaning windows. Unfortunately, TiO_2 absorbs only a fraction of sunlight, which limits its usage. Therefore, it would be technologically and economically advantageous to shrink the titania band gap. One widely proposed method to enhance the absorption properties of titania is to introduce additives. It is expected, that by using an impurity-containing material a more efficient self-cleaning window can be prepared.

Stainless steel is widely used in numerous applications. Although stainless steel is highly resistant to corrosion, in some specific applications even a more advanced passive oxide layer on the surface of austenitic stainless steel is needed. One possibility to achieve enhanced resistance to inter-granular corrosion is to introduce the elements to stainless steel, which form corrosion-durable carbides (e.g. TiC). In this way custom grade stainless steel with an enhanced passive layer can be prepared. To gain deeper knowledge about the passive layer formation on stainless steel, surface studies in a controlled environment are needed.

The original contribution of the work is divided into two main parts. In the first part pristine, cobalt- and nickel-containing titania films are investigated with the aim to clarify the following points:

- 1) Phase composition of pristine, cobalt- and nickel-containing titania films as a function of annealing temperature;
- 2) The influence of cobalt and nickel addition on the properties of titania grains, crystallites, film surface roughness and light-induced hydrophilic properties;
- 3) Cobalt and nickel incorporation/segregation in doped titania as a function of annealing temperature;
- 4) Oxidation state of cobalt, nickel and titanium in films;
- 5) The influence of the substrate ($\text{SiO}_2/\text{Si}(100)$ (i.e. with native oxide layer) and HF-etched $\text{Si}(100)$ (i.e. without native oxide layer)) upon the properties of nickel- containing titania films.

A future perspective is to prepare more efficient self-cleaning windows.

The second part of the work covers the investigation of thin chromium-rich oxide film (i.e. protective oxide layer) on the surface of stainless steel obtained by surface oxidation. The aim of this study was to clarify the following points:

- 1) Comparably to apply XAS and XPS to investigate the 2p edges of metal in order to determine the chromium-rich oxide formation on the surface of stainless steel after different degree of surface oxidation;
- 1) To study the oxidation states of major and minor elements on the surface of stainless steel after using different oxygen exposures in ultra-high vacuum;
- 2) To investigate titanium carbide formation in the surface layer.

A future perspective is to prepare custom-grade stainless steel with higher corrosion resistance.

3. OVERVIEW OF TITANIA AND STAINLESS STEEL

3.1. Titania

3.1.1. General remarks about titania

Titanium is a transition metal and it is one of the world's most common metals and ninth most common element [11]. It can form different oxides, usually TiO , Ti_2O_3 and TiO_2 . Thermodynamically most stable one is TiO_2 [25]. Titania has many practical applications. Most of produced TiO_2 is used as pigment in white paints, plastics and papers. TiO_2 has also been applied in textiles, food colouring (E171) and pharmaceuticals (e.g. UV absorber in sunscreens, tablet coatings, toothpastes).

TiO_2 has three main polymorphs: rutile (tetragonal), anatase (tetragonal) and brookite (orthorhombic). The unit cells of rutile, anatase and brookite are demonstrated in Figure 1 and some properties of bulk titania three polymorphs are shown in Table 1. In Figure 1 crystal lattices are shown in the term of TiO_6 octahedra. Black atoms are titanium atoms and gray ones belong to oxygen. Light lines, which connect oxygen atoms, demonstrate octahedra edges. Three crystal structures differ by the distortion of each octahedron and by the assembly patterns of octahedral chains.

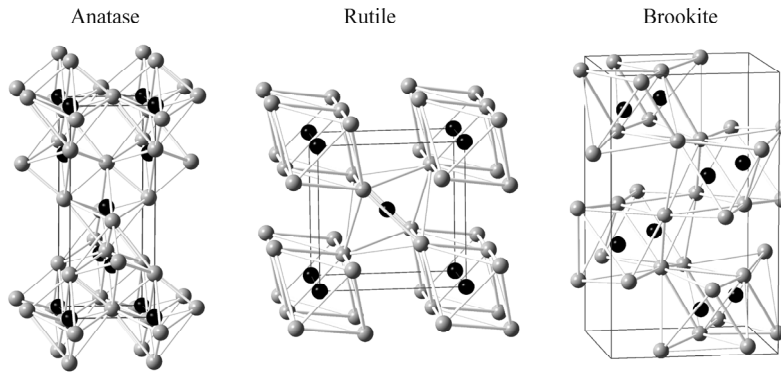


Figure 1. Crystal structure of anatase, rutile, and brookite. Black atoms are titanium atoms and gray ones belong to oxygen. Black narrow lines are unit cell edges and light lines present TiO_6 octahedron in each lattice.

Rutile is the most stable phase of titania [25]. The difference between the Gibbs free energy of TiO_2 phases exists, but it is small. This suggests that anatase and brookite are almost as stable as rutile at normal pressure and temperature. However, it has been demonstrated that the anatase is most thermodynamically stable when small TiO_2 crystallites are formed and rutile is most stable when large TiO_2 crystallites are formed [11].

In further discussion the focus will be on the properties of anatase and rutile, since pure brookite is not simply producible and it has not found much use in applications. Controversial results are reported concerning the properties of bulk brookite, therefore, some of them are marked in Table 1 with NA (not available). It is also important to note that many controversial results were reported concerning titania with metal impurities (see e.g. review paper [11]).

Table 1. Physical parameters of titania three polymorphs [26–28].

Phase	Rutile	Anatase	Brookite
Crystal structure	Tetragonal	Tetragonal	Orthorhombic
Lattice parameters, Å	$a = 4.584$ $c = 2.953$	$a = 3.784$ $c = 9.514$	$a = 9.18$ $b = 5.44$ $c = 5.14$
Density, g/cm ³	4.27	3.89	4.12
Refractive index ($\lambda = 589.3$ nm)	$n_o = 2.61$ $n_e = 2.90$	$n_o = 2.56$ $n_e = 2.49$	$n_\alpha = 2.58$ $n_\beta = 2.58$ $n_\gamma = 2.70$
Dielectric constant	89	48	78
Calculated indirect band gap (eV)	3.02 – 3.24	3.23 – 3.59	NA
Experimental band gap (eV)	~3.0	~3.2	NA
Hardness (Mohs)	6 – 6.5	5.5 – 6	NA

Anatase-to-rutile phase transition occurs in a considerable degree above 600 °C [11]. However, phase transition temperature depends on factors such as particle size, additives and lattice defects [11, 26]. The rutile is thermodynamically favoured over the anatase when the crystal size is larger. Therefore, anatase crystallite adhesion to larger particles leads to overcoming a critical nucleus size for rutile formation [11]. Additives could inhibit or promote anatase-to-rutile phase transition through the increasing or decreasing amount of oxygen vacancies in the structure. Interstitial cations decrease the concentration of oxygen vacancies and inhibit the phase transition [11]. Substitutional cations can promote or inhibit the phase transition depending on their oxidation state [11, 26]. Cations with

lower oxidation state than 4+ promote anatase-to-rutile phase transition through increasing the amount of oxygen vacancies in the lattice. Cations with higher oxidation state than 4+ are assumed to decrease the amount of oxygen vacancies. This inhibits anatase-to-rutile phase transition [26].

As can be seen in Table 1, titania's three polymorphs have several remarkable physical properties, such as high dielectric constant, high refractive index and the ability to absorb UV light. Also, titania is a chemically stable, non-toxic and low-cost material. Thanks to these properties titania (mainly anatase and rutile) has been used and studied for several high-technology applications. This covers the areas related to using titania, such as gas sensors, anti-reflection coatings, photocatalysts, anti-fogging coatings, self-cleaning coatings and biomaterials [11].

In the applications, where sunlight is collected, an effective electron-hole pair generation and a long lifetime of electron-hole pairs are required [11]. Unfortunately, titania absorbs only a fraction of sunlight. As can be seen in Table 1, its band gap depends on the crystal structure and is typically 3.2 eV in the case of anatase and 3.0 eV in the case of rutile. Therefore, it would be technologically and economically advantageous to shrink the titania band gap. However, it is important at the same time to retain the properties of titania important for the particular applications (viz. photocatalytical, light-induced hydrophilical, etc.). This is especially needed in the applications using sunlight, for example, photocatalysis and self-cleaning coatings.

An effective method for enhancing the absorption properties of titania is to dope it with anions or cations [29–32]. Impurities modify the electronic structure of the material, which can lead to more effective electron-hole pair generation and can extend the lifetime of electron-hole pairs. However, if an impurity is introduced to the material, it could also cause changes, which can reduce the material's performance, for example, its catalytic properties.

Previously it has been reported, that cobalt and nickel addition to titania has improved its catalytic properties and the absorption edge has shifted towards the visible light maximum of the solar radiation [14–16]. It has also been found that highly hydrophilic nickel-doped titania can be prepared [16]. However, cobalt and nickel additions could lead to their compounds formation and segregation. There are a number of studies related to cobalt-doped titania, where different dopant concentrations are used, but only a few works about nickel-doped titania. Very few attention has been paid to the effect of different annealing temperatures on the properties of nickel-doped films. In these investigations mainly thick films have been studied. It has been reported that doping titania with less than 4 atomic % of cobalt and annealing films below 600 °C leads to cobalt incorporation to anatase [14, 18]. When cobalt content is increased to more than 5 atomic % and annealing is still carried out below 600 °C, Co₃O₄ is formed besides anatase [18, 19]. More than 1.5 atomic % of cobalt in titania and annealing at 800 °C leads to the formation of CoTiO₃ besides rutile [14, 18]. CoTiO₃ formation besides rutile/anatase is shifted to lower temperatures when cobalt concentration is increased (above 1.5 atomic %). In the case of titania

doped with nickel, a possibility of NiO and NiTiO₃ formation besides crystal phases of titania has to be considered. NiO is a stable phase and could appear besides anatase when lower annealing temperatures are used. The formation of NiTiO₃ is favoured, when higher annealing temperatures are used. It has been demonstrated that up to 10 mole % of nickel can substitute titanium in a titania lattice when films are annealed below 500 °C [16]. However, NiTiO₃ can be formed beside titania after adding about 10 atomic % of nickel and annealing at 600 °C [33]. Nickel compound formation in films is strongly promoted with the increase of impurity concentration. When 22 atomic % of nickel is introduced to titania, NiO is formed in the films annealed at 400 °C and NiTiO₃ in the films annealed at 550 °C [34].

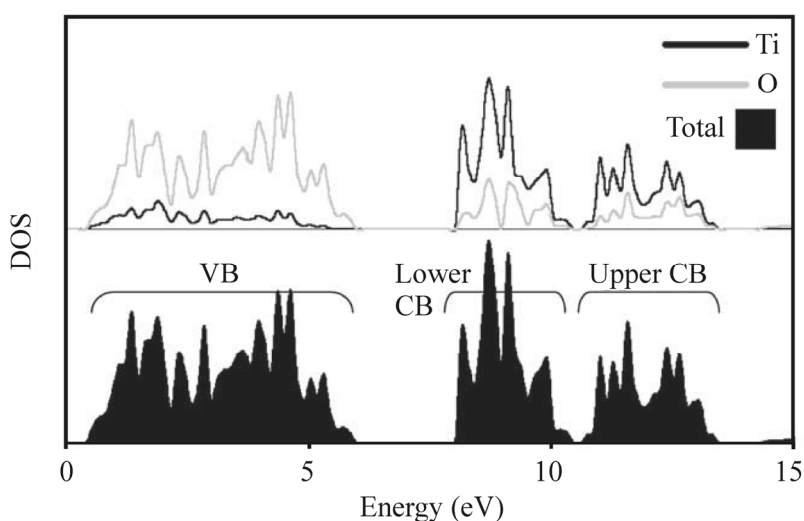


Figure 2. Total and partial DOS of rutile single crystal, DOS is divided into two parts, Ti (black line) and O (grey line) components [35].

Impurities can cause changes in the light absorption properties of titania, which have also been reported in literature [14–16]. In pristine titania UV-visible light absorption occurs, when photon excites an electron from the valence band (VB) to the conduction band (CB). VB of titania is composed of filled O 2p orbital interacting with Ti 3d. CB contains unfilled Ti 3d interacting with O 2p. Ti 3d band is split into two parts t_{2g} and e_g . In Figure 2 TiO₂ (rutile) density of states (DOS) is demonstrated. VB and CB both contain Ti 3d and O 2p orbitals. Due to Ti 3d splitting, CB is split into two parts (upper and lower CB) [35].

When cobalt and nickel impurities are introduced to titania, additional energy levels are created. Cobalt addition creates an additional energy level (t_{2g}) at the top of VB. Cobalt e_g is split into two parts and it positions in the band gap. In the case of nickel, Ni 3d band t_{2g} orbital has been found to be

delocalized and being in VB. The energy levels due to Ni e_g state are localized in the band gap [35].

3.1.2. Photocatalysis

Photocatalysis is one of the most important light-induced processes. Photocatalytic activity of titania was discovered in 1960-s by Fujishima and Honda [36]. They demonstrated that water could be split into hydrogen and oxygen by using a photoelectrochemical cell. Their studies were followed by Frank and Bard investigations of possibilities how to use titania photocatalyst to decompose cyanide in water [37]. Since then titania has achieved a lot of attention as a most important photocatalyst.

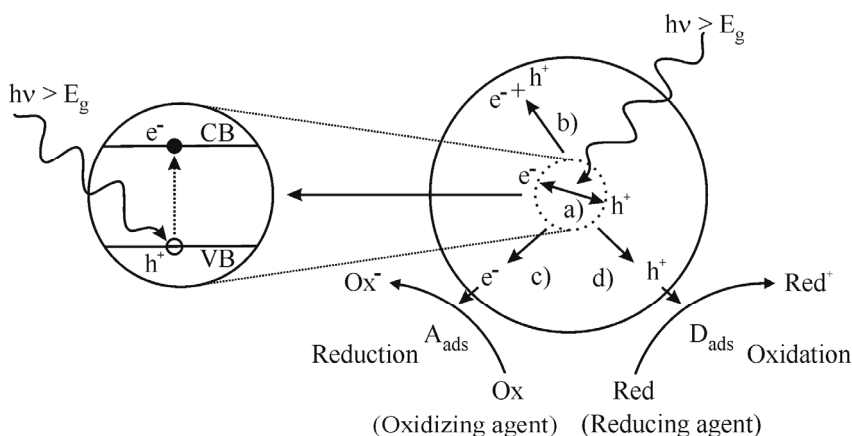
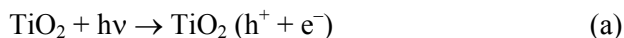


Figure 3. General processes occurring after photoabsorption: (a) electron (e^-) and hole (h^+) generation; (b) electron and hole recombination in the bulk or on the surface; (c) electron transportation to the surface, electron transfer to adsorbed acceptor (A_{ads}) and reduction (oxidizing agent electron acceptance demonstrated as $Ox \rightarrow Ox^-$); and (d) hole transportation to the surface, hole interaction with adsorbed donor (D_{ads}) and oxidation (reducing agent oxidation demonstrated as $Red \rightarrow Red^+$). The Figure has been prepared on the basis of reference [11].

In general photocatalysis is a phenomenon, where both light and catalyst are necessary to carry out or to accelerate chemical transformations [38]. The processes occurring in a semiconductor after photoabsorption are demonstrated in Figure 3. Photocatalysis is activated by the absorption of a photon ($h\nu$) the energy of which is larger than the band gap of the semiconductor (in our case titania). As a result, the electron (e^-) is excited to CB, and a hole (electronic vacancy, h^+) is left to VB. This process is demonstrated in Figure 3 (a). It could occur that the generated electrons and holes recombine, and cannot be used to

promote chemical transformations (Figure 3 (b)). However, if the lifetimes of electrons and holes are sufficiently long, they can diffuse to the surface and can be used to carry out redox reactions (Figure 3 (c) and (d)). Another crucial factor for a semiconductor photocatalyst is the position of CB and VB relative to the Fermi level. This determines the oxidizing power of holes and the reducing power of electrons. In the case of titania, the band positions have been found to be suitable for photocatalysis. On the surface of TiO₂ photogenerated holes can oxidize H₂O molecules or surface hydroxyl groups (OH⁻) to produce hydroxyl radicals ([•]OH) according to the following reactions [39, 40]:



In the presence of oxygen, electrons are utilized to reduce oxygen (O₂) and form superoxide ([•]O₂⁻) ions. These species subsequently can react with protons and adsorbed H₂O and produce hydroperoxide radicals ([•]HO₂). Hydroperoxide radicals can form hydrogen peroxide (H₂O₂). Hydrogen peroxide can react with [•]O₂⁻ to produce more [•]OH radicals. The formations of these groups can occur according to the following reactions [39, 40]:



After photoabsorption, reduction and oxidation can lead to the formation of such species on surface as holes, H₂O₂, [•]O₂⁻, [•]HO₂ and [•]OH. These are highly reactive and can oxidize a large variety of organic compounds [39, 40].

On comparing the photocatalytic activity of anatase and rutile it has been proposed that anatase has higher activity than rutile. It has been suggested that this is due to anatase's higher ability to adsorb oxygen, lower rate of electron-hole pair recombination and higher number of hydroxyl groups on the surface [39].

3.1.3. Light-induced hydrophilicity

Light-induced hydrophilicity is another important property of titania. This process appears relatively independent of photocatalysis, however the first step (electron-hole creation) is the same. The light-induced hydrophilic titania surface was first reported in literature by Fujishima in 1997, when he and his colleagues published their findings in Nature [3]. This has been followed by an intensive study of undoped and doped titania surfaces with the purpose to prepare anti-fogging coatings on transparent substrates, for example, on glass.

The mechanism of light-induced hydrophilicity is demonstrated in Figure 4. Light-induced hydrophilicity is activated by a photon the energy of which is larger than the band gap of a semiconductor. As a result of photon absorption, an electron is excited to CB, which leaves a hole into VB [11]. It is crucially important that the recombination rate of electrons and holes should be small and that they could diffuse to surface. Then photogenerated electrons reduce Ti^{4+} cations to Ti^{3+} and simultaneously holes are trapped at lattice sites or close to the surface of titania. Trapped holes weaken the bond between the associated titanium and the lattice oxygen, allowing oxygen to liberate, and through this create oxygen vacancies. Then, on these surface vacancies dissociative water absorption occurs: as a result the surface becomes more hydroxylated.

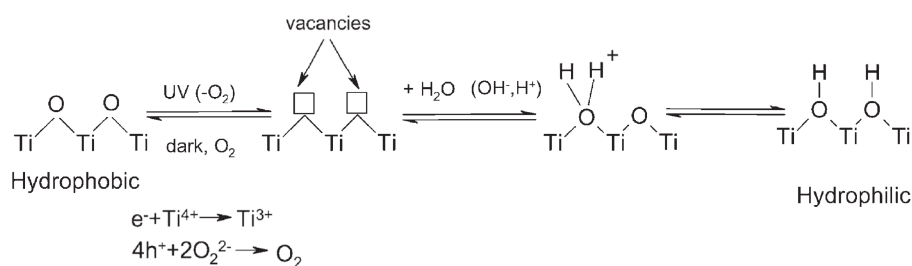


Figure 4. Simplified mechanism of light-induced hydrophilicity [11].

An increased amount of ^-OH groups on the surface leads to the increase of van der Waals forces and hydrogen bond interactions between the adsorbed H_2O and surface hydroxyl groups. As a result, water droplets spread over the surface [11]. Usually it occurs in the way that the longer the surface under UV light is, the smaller is the contact angle of the water droplet. The surface is called superhydrophilic when, after placing water droplet on the surface, it takes an irregular shape and the contact angle between the droplet and the surface is close to zero degree. In Figure 5 a water droplet on the surface of nickel containing titania before and after 6 min under UV illumination is demonstrated.

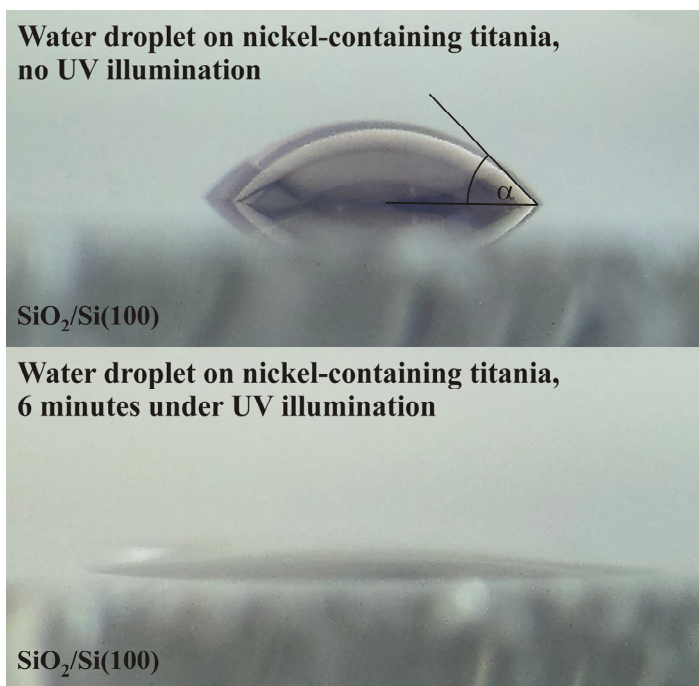


Figure 5. Water droplet on nickel containing titania prepared on SiO₂/Si(100) substrate before and after 6 min under UV illumination. Contact angle is marked with alpha.

Light-induced hydrophilicity can be accompanied by photocatalytic activity, which makes it possible to prepare self-cleaning windows. It is important to note that the self-cleaning of windows works as a two-step process: (i) photocatalytic degradation of organic and inorganic pollutants, and (ii) washing away the products of degradation (even through naturally occurring rain). Due to the light-induced superhydrophilicity the washing is very effective.

3.2. Stainless steel

Since the discovery of stainless steel in the beginning of 20th century it has widely been used in a number of applications, for example, tableware production, food industry, medicine, chemistry, automotive technology, etc. It is all due to its excellent corrosion resistance in oxidizing environments, good physical and mechanical properties.

Steel is made stainless by adding more than 11 weight % of chromium to iron. However, when impurities are introduced to the alloy (for example nickel), it is necessary to increase the chromium content significantly above 11 weight %. Maximum chromium content in alloys could be even 30 weight %. Yet, to

call this alloy steel, the iron content beside all additives and chromium has to remain over 50 weight % [10].

Stainless steels can be divided into many categories, each containing a number of specific types with its own characteristics. Most common stainless steels are ferritic and austenitic. Ferritic stainless steel has a body-centered cubic (bcc) structure, bcc unit cell is demonstrated in Figure 6 (a). In principle, ferritic stainless steel is a binary alloy containing a little bit more than 11 weight % of chromium besides iron. This alloy is magnetic [10, 41]. Austenitic stainless steel has a face-centered cubic (fcc) structure, fcc unit cell is demonstrated in Figure 6 (b). To achieve the austenitic structure (fcc), the elements called austenitizers have to be added, most commonly nickel. However, manganese and nitrogen are also known as austenitizers. Most common austenitic stainless steel contains 18 weight % of chromium and 8 weight % of nickel. Austenitic stainless steel has good corrosion resistance, good mechanical properties and it is non-magnetic [10, 41]. Other common stainless steels are martensitic and duplex.

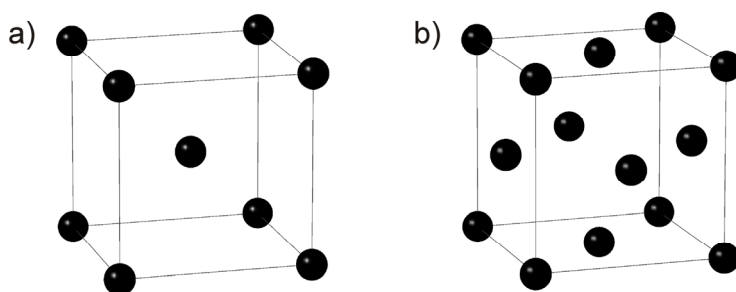


Figure 6. Unit cells: (a) bcc (e.g. ferritic) and (b) fcc (e.g. austenitic).

The key issue related to stainless steel corrosion resistance is the protective chromium-rich surface oxide layer. This suppresses the ion diffusion between the alloy and the ambient environment and protects the alloy from further corrosion. Typical thickness of the protective oxide layer is 1 – 3 nm [42]. This thin layer, under appropriate conditions, is also self-repairing. In some specific applications even more advanced passive oxide layer on the surface of austenitic stainless steel is needed. High-temperature corrosion resistance has improved, when Si and Mo are added to stainless steel [17].

Stainless steel materials are composed of crystallites. Usually, crystallites are in size of tens of micrometers. Between crystallites grain-boundaries are formed. It has been widely known that there occurs chromium carbide segregation to grain-boundaries. Since chromium carbides are not durable to oxidation, a cracking of stainless steel could appear in the grain boundary region. One possibility to reduce chromium carbide formation is the adding of other elements to stainless steel, which form oxidation-resistant carbides. It has

been demonstrated that titanium is one of such elements [12, 13]. Titanium carbides, which are more oxidation-resistant, preferably replace chromium carbides on grain boundaries. However, to obtain titanium carbides the alloy has to be annealed. In this way custom-grade stainless steel with an enhanced passive layer can be prepared.

4. THIN FILM PREPARATION

4.1. Sol-gel method

The sol-gel method is a well-established technique for preparing films, powders, etc. Often the sol-gel method has a number of advantages over other preparation techniques, such as flexibility in introducing impurities in large concentrations, homogeneity, stoichiometry, ability to coat large and complex surfaces, and cost-effectiveness [11].

The sol-gel method is a wet-chemical technique. In a very simplified scheme, the process starts with solving a precursor (in our case titanium(IV) butoxide) in a solvent. The precursor is partially hydrolysed by adding a water-solution, which initiates hydrolysis and condensation reactions. Condensation results in the formation of colloidal particles or macromolecules. Further condensation leads to the formation of porous 3-dimensionally interconnected solid networks (gels). Gels can be colloidal (formed from colloidal sol) or polymeric (formed from subcolloidal units). The next step is drying, where the solvent is mostly evaporated and removed. To obtain a crystal structure and remove the last of organics from the material usually annealing is used [43, 44].

Many types of precursors can be used for sol-gel deposition. However, usually non-alkoxides (for example inorganic salts) or metal alkoxides are utilized. In order to prepare titania, $\text{Ti}(\text{O-E})_4$, $\text{Ti}(\text{I-OP})_4$ and $\text{Ti}(\text{O-nBu})_4$ are most commonly used [11].

Films are made by the sol-gel method, mainly by using dip-coating or spin-coating techniques. Dip-coating involves an immersing the substrate into the precursor solution and pulling out the substrate. Thereat gravitational force removes the redundant material. Spin-coating is a method, where sol is coated onto the rotating substrate. Centrifugal force removes the redundant material and thin precursor films are formed.

4.1.1. Preparation of undoped, cobalt- and nickel-containing titania films

In this work, the characterization of samples was in the focus, not the film preparation. Therefore, the film preparation is described briefly. For the current investigations pristine, cobalt- and nickel-containing sol-gel titania films were prepared by Urmas Joost.

Pristine, cobalt- and nickel-containing titania thin films were prepared by sol-gel method by using commercially available titanium(IV) butoxide (Vertec, purity 98 %), cobalt nitrate hexahydrate ($\text{Co}(\text{NO}_3)_2 \cdot 6\text{H}_2\text{O}$, Alfa Aesar, purity 99.95 %) and nickel chloride hexahydrate ($\text{NiCl}_2 \cdot 6\text{H}_2\text{O}$, Alfa Aesar, purity 99.95 %). Since the compounds are sensitive to water, the solvent (butanol) was dried by using CaH_2 and distilled prior to utilization.

The precursor material for pristine titania was prepared by partial polymerisation of titanium(IV) butoxide. The molar ratio of water to titanium(IV) butoxide was chosen 1.4. The precursor material for cobalt- and nickel-containing titania was prepared by a partial polymerization of titanium(IV) butoxide, where nickel chloride hexahydrate or cobalt nitrate hexahydrate was introduced together with water/butanol mixture. Water in $\text{NiCl}_2 \cdot 6\text{H}_2\text{O}$ or $\text{Co}(\text{NO}_3)_2 \cdot 6\text{H}_2\text{O}$ was taken into account when calculating the water/titanium(IV) butoxide ratio. PH was adjusted with hydrochloric acid to catalyse polymerisation. The atomic ratio of Ni and Ti (Co and Ti) in the precursor was 1:24. Although the average atomic ratio for whole sample did not change during the subsequent annealing, it was possible that spatial redistribution of impurity atoms occurred during the heating. The annealed films contained approximately 4.2 atomic % of nickel or cobalt relative to titanium.

The polymerized alkoxide solution was concentrated at a lowered pressure of 500 Pa at 60 °C. Evaporation procedures were conducted on the Büchi R-114 Rotavapor installation equipped with a two-stage membrane vacuum pump and an electronic vacuum controller. A solution containing 11.0 mass % of the concentrate in butanol was used as a precursor for the film deposition.

Thin films were prepared by spin-coating on methanol-cleaned Si(100) (i.e. with native oxide layer) and quartz substrates in the ambient atmosphere. Nickel-containing titania films were also prepared on HF-etched Si(100) (i.e. without native oxide layer).

The rotation frequency during the spin-coating was 5000 rpm and the coating time was 0.5 min. The obtained precursor films were aged at room temperature in ambient conditions for 4 days. The purpose of such aging was to allow the remaining solvent to evaporate at a lowered pace in order to prevent the cracking of the films.

The remaining organic solvent was evaporated from the material and crystallites were formed during the heating of the samples in a furnace (in air). For annealing the furnace Nabertherm HTR70–150/13 was used. Annealing regimes are demonstrated in Figure 7. At the beginning all eight samples were put into the furnace, then the temperature was increased to the first set value of 450 (or 500) °C by using the ramping rate 2.4 (or 2.6) °C/min. In order to obtain a good reproducibility the samples were annealed for one hour at a constant temperature. It was assumed that during that time the equilibrium was reached in the phase composition and crystallite growth. After a one-hour dwelling time, one sample was removed from the furnace and then the temperature was increased to the next desired value (550 °C or 600 °C) by using a ramping rate 1.7 °C/min. This was followed by the annealing for one hour at that temperature and the removal of the sample from the furnace. The procedure was repeated until the last sample was removed from the furnace after a one-hour annealing at 1150 (1200) °C.

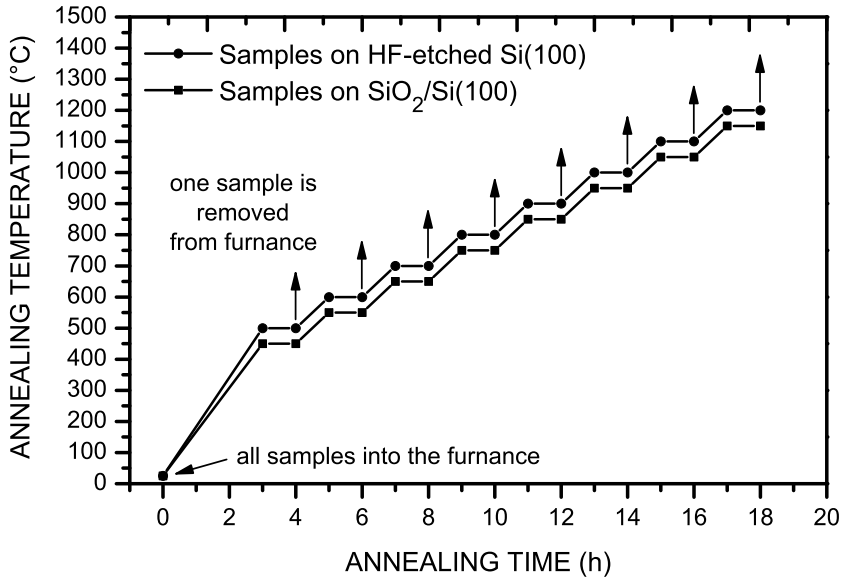


Figure 7. Annealing regimes of the samples. Each arrow marks the time moment when one sample was removed from the furnace.

4.2. TiC-enriched austenitic stainless steel preparation and surface oxidation

An austenitic stainless steel sample was studied together with colleagues from Tampere University of Technology. In collaboration, surface pre-treatment and oxidation experiments were carried out.

The stainless steel sample was produced in Outokumpu Stainless Oy (Tornio, Finland). The chemical composition of the bulk alloy used, resembles closely (but not fully) grade UNS S33400 [45] and consists of: 60.1 at.% Fe, 19.4 at.% Cr, 17.5 at.% Ni, 1.0 at.% Al, 0.5 at.% Mn, 0.7 at.% Si, 0.4 at.% Ti and 0.24 at.% C. Furthermore, the alloy contains a very low concentration of non-metals and traces of metals typical of industrial melts (mainly O, N, S, P, K and W).

The TiC-enriched surface was prepared by annealing the bulk alloy to 727 °C. After this treatment the amount of TiC remained constant throughout several cleaning cycles. The relative atomic surface concentrations of minor alloy constituents after each cleaning were 12 – 20 % Al, 8 – 18 % O, 7 % C, 7 % Ti and 1 – 2% Si within the XPS analysis depth when using a photon energy of 400 eV.

Oxidation experiments were performed by backfilling the UHV chamber (base pressure 1×10^{-10} mbar) with 2.7×10^{-6} mbar of O₂ (99.9999 %), while maintaining the sample temperature 50 °C throughout the exposure duration. The investigated O₂ exposure range was 0 – 3000 L (1 L = 10^{-6} Torr·s).

5. X-RAY ABSORPTION

5.1. X-ray absorption spectroscopy

X-ray photons interaction with matter leads to absorption and scattering processes. The strength of these interactions can be quantified in terms of cross-sections. The cross-sections of different processes occurring during x-ray photons interaction with matter (in copper) are demonstrated in Figure 8. In the case of soft x-rays (photon energy < 2 keV) the photoelectric absorption leading to the emission of photoelectrons dominates by orders of magnitude over all other interactions of soft x-ray photons and matter such as elastic and inelastic scattering [21, 46].

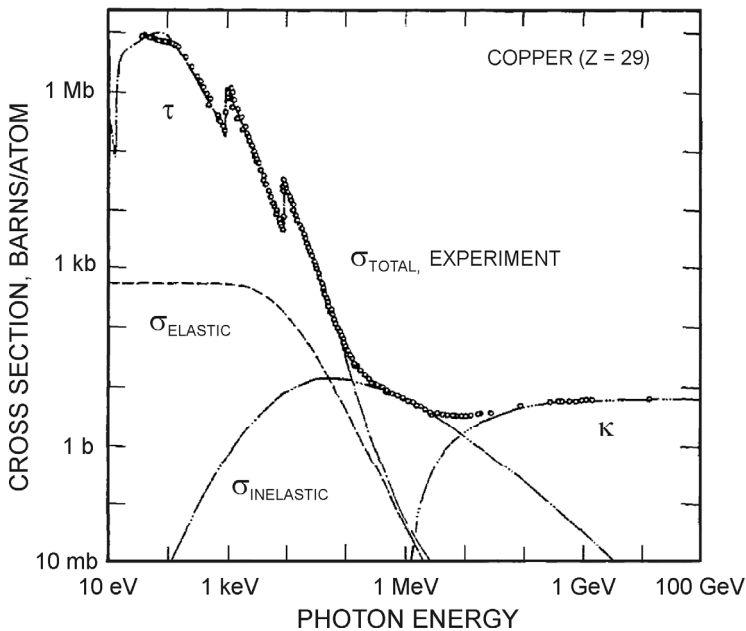


Figure 8. Contribution of atomic photoeffect (τ), elastic scattering (σ_{ELASTIC}), inelastic scattering ($\sigma_{\text{INELASTIC}}$) and pair production (κ) to total cross-section in copper over photon energy range of 10 eV to 100 GeV. Cross-section is given in barns/atom (barn = 10^{-28} m²). Figure is prepared on the bases of reference [47].

In x-ray absorption spectroscopy (XAS) the measurable physical quantity is an x-ray absorption coefficient, also called a linear absorption coefficient. It describes how strongly x-ray photons are absorbed as a function of x-ray photon energy. The absorption coefficient is related to the x-ray absorption cross-section linearly by the atomic volume density of the sample. Generally, the x-ray absorption coefficient decreases when the x-ray photon energy increases. However, in certain x-ray photon energies the x-ray absorption coefficient

increases abruptly. This occurs when the x-ray photon energy becomes equal to a specific energy (binding energy of some core level) and electron liberates from atom. This sudden increase of the absorption coefficient is called absorption edge [21, 46]. Figure 8 demonstrates the change of the cross-section of x-ray absorption in copper as a function of photon energy. A generally smooth decrease of x-ray absorption and sharp increases at photoabsorption edges are well observable.

The absorption of x-ray photons leads to the formation of photoelectrons when the x-ray photon energy is higher than the electron binding energy in an atom (relative to Fermi level). After photoionization a hole is left in that electron energy level. This hole can be filled with an electron from the upper energy level simultaneously by the ejection of another electron (Auger effect). Alternatively, the hole can be filled by an electron and an x-ray photon is emitted. The radiative and the Auger decay processes compete with each other. The strength of the radiative decay or the Auger decay depends strongly on the atomic number. For the K-shell excitation of low- Z atoms ($Z < 30$) and L-shell excitation of all atoms ($Z < 90$) the Auger decay is faster and hence dominates [21].

Photoionization and relaxation of the core hole through the Auger effect is demonstrated in Figure 9 (a). Although the emission of x-ray photon or the ejection of Auger electron (Auger electron decay) are followed by photoionization, similar processes occur when an electron is excited to localized unoccupied energy level (photoexcitation). In that case no primary electron ejection occurs – the excited electron is localized at the absorption site. Thus, XAS probes both the localized and the unlocalized unoccupied states. The photoexcitation followed by the Auger decay is demonstrated in Figure 9 (b). The Auger decay can happen in two ways: the excited electron participates in the relaxation process (participator Auger transition) or it retains its state (spectator Auger transition).

Two regions in x-ray absorption spectra can be separated: the edge and the extended edge. This gives also names to the two main techniques in XAS. The edge region is studied with near edge x-ray absorption fine structure spectroscopy (NEXAFS), also called as x-ray absorption near edge spectroscopy (XANES). It involves the energy region from about 10–20 eV below the edge to about 30–40 eV above the edge, where the rapid changes of absorption coefficient (cross section) can be observed. It probes directly unoccupied states. The photon energy region 100 – 1000 eV above the edge is called extended x-ray absorption fine structure (EXAFS). EXAFS structure is formed from the destructive and non-destructive interference of scattered electrons from neighbouring atoms. By using numerical methods it is possible to calculate interatomic distances from EXAFS spectra.

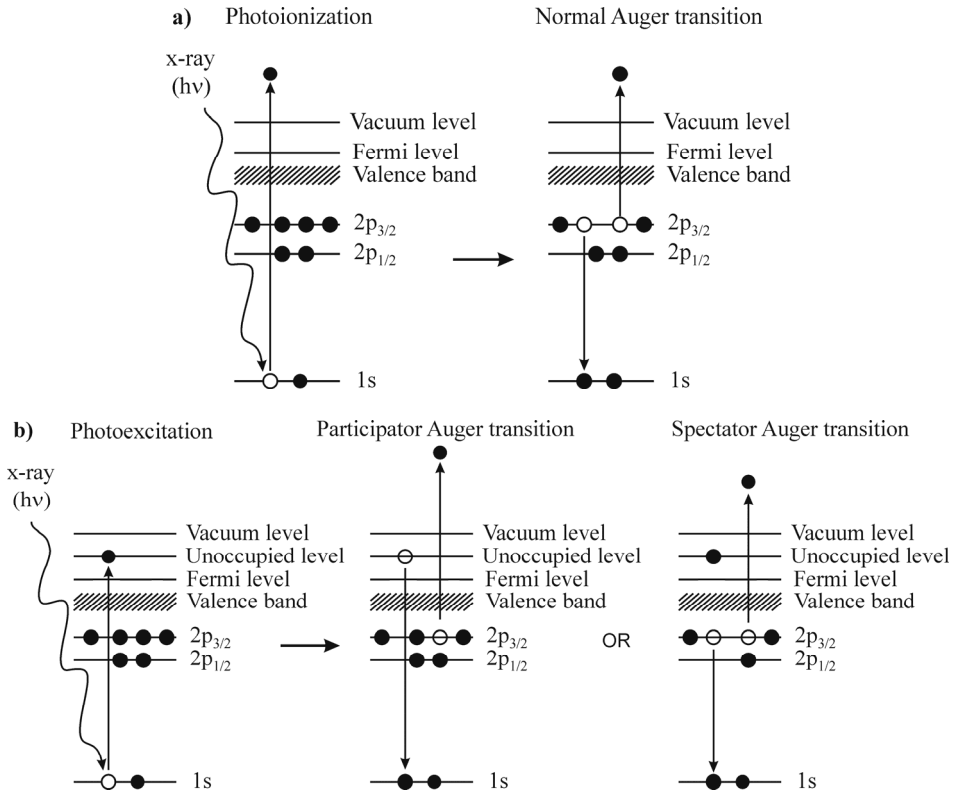


Figure 9. Processes occurring in x-ray absorption: (a) photoionization leading to the emission of photoelectron and relaxation of created core hole by normal Auger transition, (b) photoexcitation, which leads to the participator or spectator Auger transition.

Typically x-ray absorption can be measured in several modes: transmission, fluorescence yield and electron yield. Transmission mode is most straightforward: it simply involves the measuring of the x-ray photon flux before and after the beam is passed through the sample. However, it can be used only in the case of hard x-rays, because of the small penetration depth of soft x-rays in matter. X-rays with photon energy between 100 and 1000 eV have penetration depths from tens of nanometers to a couple of microns, depending on the material. For example, in the case of iron it is 22 nm for x-rays with photon energy of 100 eV and 140 nm for x-rays with the energy of 1000 eV [48]. The preparation of freestanding samples with such a small thicknesses is very difficult and, therefore, in a soft x-ray region fluorescence and electron detection is feasible. In fluorescence yield measurements the x-ray photons emitted after photoabsorption are detected and in the electron yield the electrons emitted after photoabsorption are measured [46]. The use of these yields for x-

ray absorption measurements is based on the circumstance that the electron and fluorescence yields are proportional with x-ray photoabsorption cross-section.

Electrons can be measured in different modes: total electron yield (TEY), partial electron yield (PEY) and Auger electron yield (AEY) mode. In TEY mode electrons with all kinds of kinetic energies are detected [21]. In PEY mode, only these electrons are detected, which have their kinetic energy in the region defined by the experimenter. As a special case of PEY mode, often the AEY is used, when the energy window is adjusted so that only Auger electrons are detected.

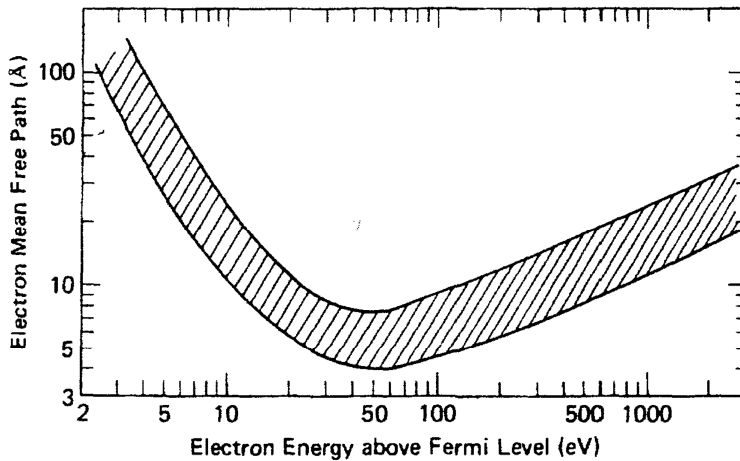


Figure 10. Typical electron mean free path in solids as a function of the electron kinetic energy above the Fermi level. The shaded area represents the distribution typically found for different materials [21].

X-ray absorption leads to the creation of photoelectrons and Auger electrons. The electron mean free path as a function of electron kinetic energy follows a “universal curve”, demonstrated in Figure 10. There the shaded area represents the distribution, which is typically found for different elements. The smallest electron mean free path in solids, less than 10 Å, is for the electrons the kinetic energy of which is around 50 eV. On their way to the surface electrons scatter inelastically, creating new electrons with lower energies and leading to the formation of an electron cascade. When new electrons have energies below the band gap, they cannot create new electrons and will lose energy in the case of scattering on phonons. As these electrons will lose small amounts of energy in scattering, they can travel long distances before reaching the surface. Thus the measuring of low-energy secondary electrons will give the largest probing depths.

5.2. X-ray photoelectron spectroscopy

X-ray photoelectron spectroscopy (XPS) is based on a photoelectric effect. The sample is irradiated by using x-rays with fixed photon energy, this causes an emission of photoelectrons from the sample surface. In the case of solids the kinetic energy of an excited electron has also to overcome the surface energy potential (work function) in order to emit. The process of photoemission is shown schematically in Figure 9 (a) left. When the number of emitted electrons is measured as a function of their kinetic energy (E_K), then photoelectron spectra are obtained. Knowing the photon energy ($h\nu$) and the work function of a solid (Φ), one can determine the electron binding energy (E_B) in the sample according to following equation [49]:

$$E_B = h\nu - E_K - \Phi$$

XPS is known as a surface-sensitive technique. Surface sensitivity of XPS comes from a small electron mean free path in materials. The electron mean free path in solids as a function of the electron kinetic energy above the Fermi level is demonstrated in Figure 10. The shaded area represents the distribution typically found for different elements. As one can see, when using soft x-rays (photon energy < 2 keV), the electron mean free path in solids is mostly less than 2 nm for majority of elements [49].

XPS is a good tool to identify elements on the surface layer, since all elements have their core levels at specific energies as compared to each other. Also, XPS is a good tool to determine the chemical state of surface atoms. For example, electrons in metal have certain Columbic interaction between the nucleus and electrons. When oxide is formed, metal transfers its electron to oxygen due to its larger electronegativity. This results as a stronger Columbic interaction between the nucleus and electrons. Therefore, the binding energy of electron is larger in metal oxide than in metal and a “chemical shift” between two compounds is observed [49].

In photoelectron spectra also other structures, besides photoelectron peaks, are present. Usually, the bands related to Auger structures, but also to shake-up satellites, shake-off satellites and multiplet splitting can arise. The Auger electron decay mechanism was introduced in the previous section. However, it should be added that Auger transition is an inner atomic process and the Auger electron kinetic energy does not depend on photon energy as does the photoelectron kinetic energy. Shake-up satellites are formed, when the outgoing photoelectron simultaneously interacts with a valence electron and excites it to a higher-energy level. This process leads to the decrease of the energy of the ejected core electron and satellites appear in photoelectron spectra. Shake-up satellites are few electron volts below the core level position. This process can be accompanied by the formation of a shake-off satellite. The shake-off satellite is formed in the way that a valence electron is ejected from the ion [20]. A multiplet splitting may arise in a compound that has an unpaired electron in the

valence band. When a core hole is created through photoionization, there can be coupling between the unpaired electron in the core shell with an unpaired electron in the outer shell. This can create a number of final states, which arise in the photoelectron spectrum as a multipeak structure [20].

6. EXPERIMENTAL

6.1. Synchrotron radiation

Large scale facilities, where relativistic electrons are moving in a circular orbit and emit synchrotron radiation, are called synchrotrons. This light (synchrotron radiation) is very bright, polarized and emitted in a wide spectral range [50]. A schematic of synchrotron ring with one beamline is shown in Figure 11.

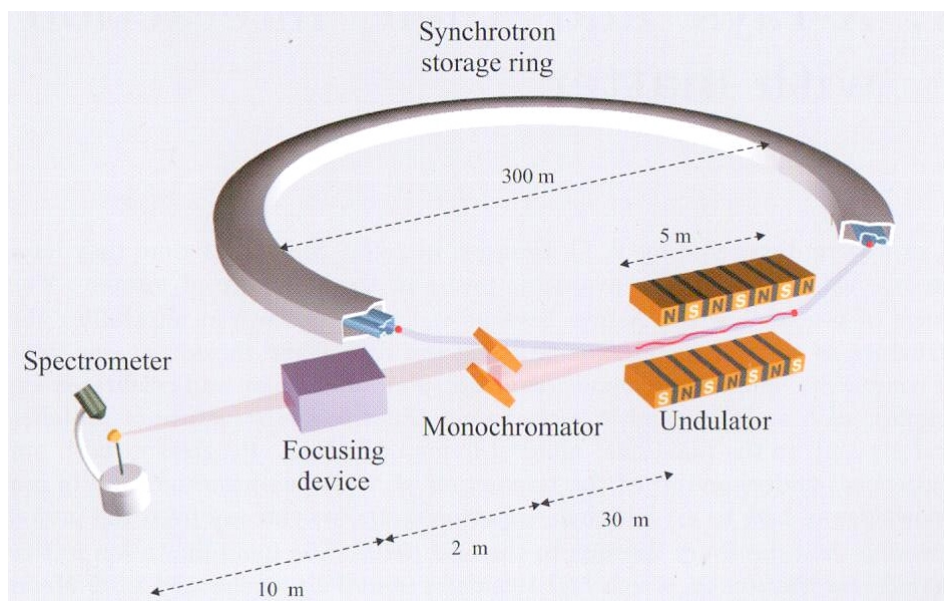


Figure 11. Schematic of a synchrotron ring with one beamline. Bunches of charged particles circulate in the storage ring. The ring is designed with straight sections, where an insertion device is placed (bending magnet is placed in the curvature part of the machine). When an electron bunch passes through the insertion device (or bending magnet) magnetic field, it is accelerated and radiation is produced. This radiation then passes through a number of optical elements, such as monochromator, focusing devices, etc., so that a beam with desired properties is delivered to the sample. Typical distances are indicated [51].

In synchrotron, radiation is produced by using two types of devices: dipole (bending) magnets or insertion devices. Dipole magnets are devices where homogeneous magnetic field is created between two poles, due to that a relativistic electron bunch is tilted. In synchrotron, bending magnets create the curved part of electron trajectories. Bending magnet radiation has a broad spectrum. Insertion devices can be divided into two main groups by the strength of their magnetic field: wigglers and undulators. In wigglers the magnetic field

is strong. In general, the wiggler acts like a sequence of bending magnets with alternating polarities. Wiggler spectrum is more intense than the bending magnet one. Undulator is also a multiperiod magnetic system. In undulator magnetic field is weak and beam deflections are small. This results in radiation interaction with itself, producing destructive and constructive interference. The undulator spectrum includes intense peaks. Insertion devices are placed to straight sections of the storage ring [50].

To bring synchrotron radiation to experimental stations, beamlines are constructed. A beamline contains a monochromator and its associated pre-focusing and post-focusing optics. A schematic of a beamline at a synchrotron is demonstrated in Figure 11.

In this work, experiments were carried out at beamline D1011 of the MAX-II storage ring in MAX-lab (National Laboratory for Synchrotron Radiation, Lund University, Sweden). Additional measurements were carried out at beamline I511-3 of the MAX-II storage ring and in the home laboratory (Laboratory of X-ray Spectroscopy, Institute of Physics, University of Tartu) with the conventional XPS apparatus.

6.2. XPS and XAS measurement systems

6.2.1. Beamline D1011

Beamline D1011 is dipole magnet beamline in the synchrotron facility MAX-lab. It has two end stations, one to measure magnetic circular dichroism and the other one to carry out photoemission and photoabsorption experiments by using linearly polarized light. Beamline D1011 is equipped with a SX-700 plane-grating monochromator. The available energy range is between 30 and 1500 eV. Photon flux on the sample is about $10^{10} - 10^{11}$ ph/s. The photoemission and photoabsorption experimental system consists of separate analysis and preparation chambers accessible via a long-travel manipulator. The analysis chamber is equipped with an electron energy analyser (Scienta SES-200) and a microchannel plate detector (MCP) for electron yield measurements. It has also a possibility to measure the sample's photocurrent during XAS measurements. The preparation chamber is equipped with low-energy electron diffraction, ion sputtering guns and a gas-inlet system [52].

6.2.2. Beamline I511

Beamline I511 is undulator-based beamline in MAX-lab. It has two end stations: one is constructed for high-pressure XPS and XAS measurements (I511-1), and the other one for XAS and x-ray emission spectroscopy (XES) measurements (I511-3). Beamline I511 is equipped with a SX-700 plane-grating monochromator. The available energy range is between 50 and 1500 eV. Photon flux on the sample is about $10^{11} - 10^{13}$ ph/s. I511-3 has a soft X-ray

emission spectrometer (Scienta XES-350) for soft XES studies of non-UHV compatible systems. XAS can be measured by using the electron yield (detecting sample current or electrons by using on-site channeltron) or the photon yield (using the XES detector or a photodiode) [53].

6.2.3. Surface station at Institute of Physics University of Tartu

The XPS system in the laboratory of x-ray spectroscopy (University of Tartu, Institute of Physics) consists of three vacuum chambers (load-lock, preparation chamber and analysis chamber). Load-lock is used to insert *ex situ* samples into the vacuum system. The preparation chamber offers possibilities to heat samples and to clean the sample surface with Ar⁺ ion sputtering. Photoemission experiments are carried out in the analysis chamber. Excitation sources are a twin-anode x-ray tube (Thermo XR3E2) and a helium lamp. The X-ray tube offers possibilities of using non-monochromatized Al K α radiation ($h\nu = 1486.6$ eV) and Mg K α radiation ($h\nu = 1253.6$ eV). A helium lamp is used as vacuum ultraviolet source, it enables us to use radiation with the energy of 21.2 eV (He I) and 40.8 eV (He II). For the detection of electron kinetic energy distribution an electron energy analyser (Scienta SES-100) was used.

6.3. XPS and XAS experimental details

6.3.1. Undoped, cobalt- and nickel-containing titania

Mainly XPS and XAS measurements were carried out at beamline D1011. XPS spectra were measured by using Scienta SES-200 in a fixed analyser transmission (FAT) mode with 200 eV pass energy. The XPS spectra were normalized to the synchrotron ring current, the binding energy scales were referenced to the binding energies of the Ti 2p_{3/2} (458.6 eV) and the O 1s (529.9 eV) photoemission lines. The XAS spectra (Ti 2p) were measured in the PEY mode by using a MCP detector with a retention voltage of 200 V. The photon energy resolution was about 0.1 eV. All the spectra were measured near the normal (4°) incidence. The XAS spectra were normalized to the gold mesh current to keep account of the variations in the x-ray photon energy flux to the sample. The photon energy scale was calibrated by measuring the kinetic energy of Au 4f photoelectrons excited by 400 eV in the first and the second order of the monochromator.

Additional XAS measurements were carried out at beamline I511-3 (Ti and Ni 2p) in TEY mode by measuring the sample current. The incidence angle for XAS measurements was 35° from the surface normal. The XAS spectra were normalized in the same way as described in the previous paragraph.

The XPS measurements of the nickel-containing titania on a HF-etched Si(100) substrate were carried out at the home lab (Laboratory of X-ray Spectroscopy). In the measurements a Scienta SES-100 electron energy

analyser was used with 200 eV pass energy (exciting photon energy was 1486.6 eV). The angle between the incoming photon beam and the axis of the electron energy analyser was 45° and the sample normal was parallel to the axis of the electron energy analyser. SES-100 was calibrated by using Au 4f photolines. The photon energy resolution of the x-ray source was about 0.8 eV (full width at half maximum) and the resolution of the electron energy analyser was about 0.3 eV.

6.3.2. TiC-enriched stainless steel

XPS spectra were measured at beamline D1011 by using Scienta SES-200 in a FAT mode with 200 eV pass energy. XAS spectra were measured in the TEY mode by using a MCP detector. The photon energy resolution was about 0.1–0.2 eV. The sample was positioned at a normal emission with 40° incident angle for the incoming photon beam.

XPS and XAS spectra were normalized to the synchrotron ring current to keep account of the variations in the photon beam intensity. The binding energy scales for XPS experiments were referenced to the Ni 3p_{3/2} (66.3 eV), 3s (110.7 eV) and 2p_{3/2} (852.7 eV) transitions. The photon energy scale for XAS experiments was calibrated by measuring the kinetic energy of Fe 3p (52.8 eV) and Ni 3p_{3/2} (66.3 eV) photoelectrons excited by photon energy of 400 eV in the first and the second order of the monochromator. The XAS spectra of metal 2p edges were normalized by a reference signal from a gold mesh. O 1s edge spectra were normalized by a cleaned alloy spectrum. For reference, cleaned Fe, Cr, Ni foils and oxidized Fe, Cr foils XAS spectra were measured.

Changes in XPS peak areas of the main alloy components were determined from XPS spectra (excitation energy 1486.6 eV). Fe 2p, Cr 2p, Ni 2p, Ti 2p and O 1s photopeaks were fitted by asymmetric Gaussian-Lorentzian lineshapes after subtracting a Shirley background. An analysis was carried out by using a CasaXPS software (version 2.3.13) [54].

6.4. X-ray diffraction

X-ray diffraction (XRD) is a straightforward method for determining the crystal structure, the orientation of crystallites and the crystallite mean size. The method is based on the elastic scattering of x-rays from a regular array of atoms.

The crystal can be considered as three-dimensional repetition of some unit of atoms. The scheme of repetition is defined through the crystal axes. In a crystalline structure it is important to indicate the magnitude and the direction of the displacement. The smallest unit which can be repeated to describe the whole crystal is called unit cell [55].

Atoms in crystalline structure may be considered as being situated on planes. By repeating these planes parallel equidistant planes are formed. These planes are characterized by using the Miller indices. By using the Bragg law, we consider diffractions in terms of a set of crystallographic planes [55]. A

schematic of x-rays scattering from crystal planes is presented in Figure 12. An x-ray with the wavelength of λ falls upon a crystal at the angle of θ with planes with the spacing d . The beam goes to the atom A in the first plane and to the atom B in the next plane, each of the atoms in the plane scatters a part of x-rays in a random direction. A constructive interference appears only between these scattered x-rays that are parallel and whose path differs exactly λ , 2λ , 3λ times, etc. [56].

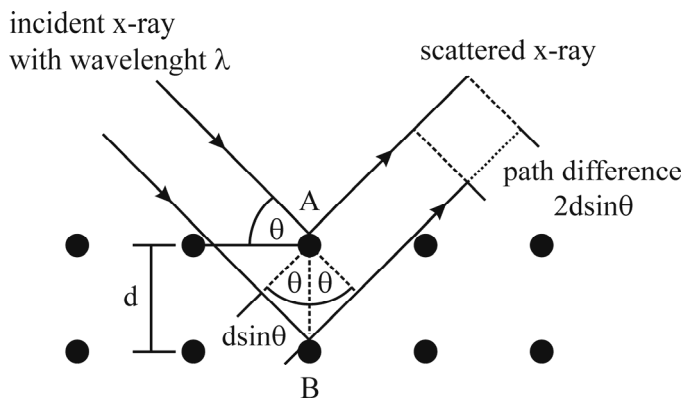


Figure 12. X-ray scattering from a crystal [56].

The Bragg law describes the occurrence of diffraction and is given as:

$$2d\sin\theta = n\lambda \quad n = 1, 2, 3 \dots,$$

where d is the distance between diffraction planes, n is integer and λ is the wavelength. Diffraction can occur only when the wavelength is smaller than $2d$ ($\lambda < d$).

6.4.1. Experimental details of x-ray diffraction

The crystalline phases of thin films were investigated by using XRD. XRD experiments were conducted by using a Bragg-Brentano x-ray diffractometer DRON-1 (Nauchpribor) operating in a symmetrical coupled $\theta/2\theta$ scanning mode, by using Cu $K\alpha$ radiation. Diffracted x-rays were measured by a scintillation detector. The scanning step was 0.02° and the measuring time for each step was 20 s. The average crystallite size was estimated from the XRD peak broadening by using the Scherrer equation [57].

6.5. Other film characterization techniques

Atomic force microscopy

Atomic force microscopy (AFM) is a good tool to obtain information about morphological properties of surfaces. By AFM the forces between the sharp tip and the surface are measured. The greatest advantage of AFM is that it gives a possibility to observe a three-dimensional surface profile. Measurements are usually carried out in atmospheric conditions (it does not need vacuum) and sample conductivity is not a crucial factor like in scanning electron microscopy.

The surface morphological changes of pristine, cobalt- and nickel-containing titania thin films were investigated by using SMENA-B (NT-MDT) AFM. Typically, the tapping mode was used in order to provide an optimal performance in such cases. From AFM images root mean square (RMS) roughness but also grain mean size were evaluated by using the Gwyddion 2.19 software [58].

Raman spectroscopy

Raman spectroscopy is a tool for studying lattice vibrations in the system. It relies on the inelastic scattering of monochromatic light from matter. In the current investigations, Raman spectroscopy was additionally applied to study lattice vibrations with a purpose to investigate the phase composition of films. The room-temperature Raman spectra of the thin films prepared on a SiO₂/Si(100) and HF-etched Si(100) substrate were measured by using the Renishaw inVia Raman microspectrometer. The wavelength of the exciting light was 488 nm.

X-ray reflection

X-ray reflection (XRR) is a method, where reflected x-rays from the sample surface are measured at small angles. It is a good method to obtain information about the film density, RMS roughness and thickness. In the present investigations the thickness of the pristine, cobalt- and nickel-containing titania films was estimated from XRR measurements by means of a modified URT-1 (Nauchpribor) diffractometer and by using Cu K α radiation. The reflection patterns were recorded in $\theta/2\theta$ scanning mode for the angular range $2\theta = 0.2 - 2.5^\circ$.

Scanning electron microscopy and energy dispersive x-ray analysis

SEM is a good method for studying surface morphology. It is based on accelerated electrons interaction with matter where the signal of secondary or backscattered electrons is detected as a function of position. Method requires a partially conductive sample (also substrate) and gives a two-dimensional image of the surface. Additionally, SEM equipment may contain an EDX detector. EDX is based on the detection of characteristic x-ray fluorescence, which is emitted after electron excitations. It gives possibilities to study the elements distribution in the sample and the sample composition.

SEM images were measured and the elemental distributions were determined by using an FIB-SEM instrument (FEI Helios 600 focused ion beam – scanning electron microscope (FIB - SEM) setup equipped with an EDX detector, Oxford Instruments). SEM images, in order to demonstrate the surface morphology of cobalt- and nickel-containing titania films, were measured at normal incidence before each EDX measurement by using an electron beam energy corresponding to 5–7 kV high voltage. SEM images, in order to demonstrate surface morphology and cross-section of the nickel containing titania films, were measured at a 50-degree angle from the film's surface by using an electron beam energy corresponding to 10 kV high voltage. In SEM measurements secondary electrons were detected.

The EDX measurements were carried out by using a primary electron beam with an acceleration voltage of 5 kV (in some cases 7 kV) to detect Ni L_{α_1, β_1} x-ray fluorescence (Ni L_{α_1} 0.851 and Ni L_{β_1} 0.869 keV), Co L_{α_1, β_1} x-ray fluorescence (Co L_{α_1} 0.776 and Co L_{β_1} 0.791 keV) and Si $K\alpha$ x-ray fluorescence (1.740 keV)

With the purpose to detect the distribution of oxygen and titanium in the cross-section of the nickel-containing titania films, EDX measurements were carried out. Firstly, the cross-section of the cut films was cleaned either with FIB (using gallium ions) or a rectangular hole was etched into the films by FIB. Then, from the cleaned areas oxygen $K\alpha$ (0.525 keV) and titanium $K\alpha$ (4.511 keV) x-ray fluorescence were measured. The excitation energy of the electron beam corresponded to 10 kV high voltage.

Optical absorption

To evaluate the optical absorption of pristine and cobalt- and nickel-containing titania, optical transmission and reflection measurements were conducted with a Jasco V-570 (UV/VIS/NIR) spectrometer equipped with a tungsten lamp and a photomultiplier. Resolution in UV-Vis region was 0.1 nm. The optical absorption coefficient α was calculated from the measured transmittance and reflectivity by using the evaluated thickness [59] obtained from XRR measurements. The optical band gap was deduced from the intersection of the extrapolated linear parts with the energy axes. Based on literature [60], it was assumed that films have an indirect optical band gap.

Light-induced hydrophilicity

The degree of the light-induced hydrophilicity was estimated by measuring the contact angle of a water droplet on the films (prepared on $\text{SiO}_2/\text{Si}(100)$ substrate), *i.e.* the angle at which the liquid vapour interface meets the solid liquid interface. The contact angle measurements were carried through by means of a sessile drop method and by using a self-made setup. The volume of the water droplets was 1.0 μL . The light source was a mercury lamp (253.7 nm, 4.89 eV). During UV light illumination the relative air humidity was kept around 90 %.

7. RESULTS AND DISCUSSION

7.1. Effect of cobalt and nickel addition to titania (Papers II-IV)

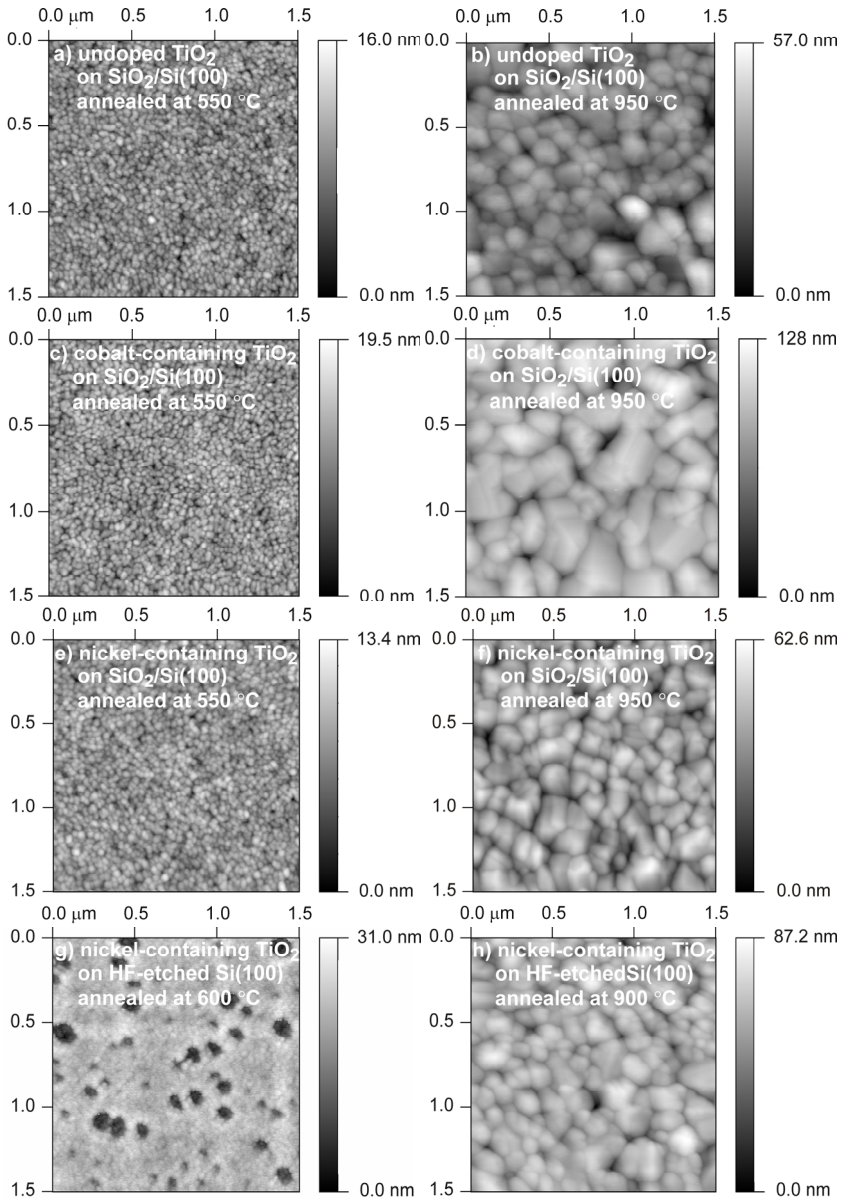


Figure 13. AFM images ($1.5 \times 1.5 \mu\text{m}^2$) of undoped titania films (a, b), cobalt-containing titania films (c, d) and nickel-containing titania films (e, f) on SiO₂/Si(100) substrate annealed at 550 °C (a, c, e) and 950 °C (b, d, f). Nickel-containing titania films on HF-etched Si(100) substrate annealed at 600 °C (g) and 900 °C (h) are comparably demonstrated. The altitude scale is shown at the right of the each image.

The AFM images (size $1.5 \times 1.5 \mu\text{m}^2$) of the pristine (undoped), cobalt- and nickel- containing TiO_2 thin films prepared on $\text{SiO}_2/\text{Si}(100)$ substrate and nickel-containing titania films on HF-etched $\text{Si}(100)$ substrate are shown in Figure 13. The films prepared on $\text{SiO}_2/\text{Si}(100)$ substrate annealed at 450 and 550 °C were rather smooth and consisted of nanometer scale grains. The grain size was about three times larger when the films were annealed at 950 °C (in the case of nickel-containing titania on HF-etched $\text{SiO}_2/\text{Si}(100)$ at 1000 °C). Further increase of the annealing temperature up to 1150 °C led gradually to the formation of films, which composed of large crystallites. Similarly to the films on $\text{SiO}_2/\text{Si}(100)$ substrate, nickel-containing titania films on HF-etched $\text{Si}(100)$ substrate consisted of nanometer scale grains after annealing at 500 and 600 °C. However, these films contained pores between crystallites when the annealing temperatures between 500 and 800 °C were used. When the annealing temperature was increased above 900 °C, these pores collapsed. In general, the films containing nickel and especially cobalt demonstrated larger grain size as compared to undoped titania films.

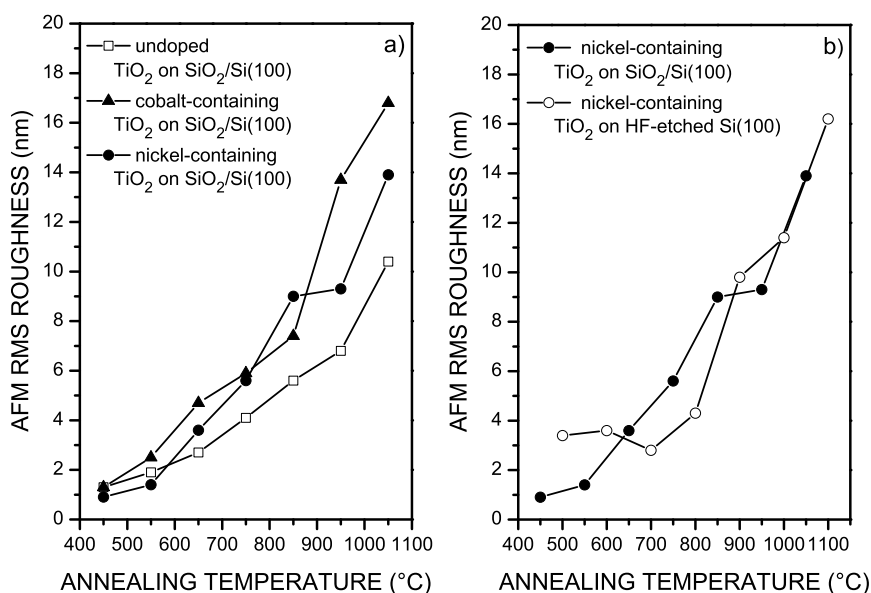


Figure 14. (a) RMS roughness of undoped, cobalt- and nickel-containing titania films on $\text{SiO}_2/\text{Si}(100)$ substrate as a function of annealing temperature. (b) RMS roughness of nickel- containing titania on $\text{SiO}_2/\text{Si}(100)$ and HF-etched $\text{Si}(100)$ substrate as a function of annealing temperature.

In Figure 14 (a), the RMS roughness of undoped, cobalt- and nickel-containing titania on $\text{SiO}_2/\text{Si}(100)$ substrate are demonstrated. A clear dependence of RMS roughness as a function of the annealing temperature can be observed. An

increase of the annealing temperature predisposes the grain growth and the formation of a rougher surface. It was found that nickel addition leads to the formation of a smoother surface as compared to pristine and cobalt-containing titania films on SiO₂/Si(100) substrate, when films were annealed at 450 and 550 °C. With the increasing of the annealing temperature above 650 °C cobalt and nickel addition led to the formation of a rougher surface than undoped titania. Nickel-containing titania on SiO₂/Si(100) and HF-etched Si(100) substrate is demonstrated and compared in Figure 14 (b). The RMS roughness of nickel-containing titania films on SiO₂/Si(100) substrate differed from the similar films on HF-etched Si(100) substrate, when films were annealed below 900 °C. This was due the pores, which were formed between nickel-containing titania crystallites. When the annealing temperature was increased above 900 °C, RMS roughness of nickel-containing films on different substrates became similar.

The XRD patterns of undoped, cobalt- and nickel-containing TiO₂ thin films prepared on SiO₂/Si(100) substrate and nickel-containing titania on HF-etched Si(100) substrate annealed at different temperatures are shown in Figure 15 ($2\theta = 24 - 29^\circ$ is demonstrated). The film aged only at room temperature did not show any reflexes in XRD pattern (not presented in Figure 15). The main reason is that an aged precursor film is not yet crystalline titania, it has an amorphous nature and it still contains traces of organic compounds (alcoxo groups and butanol). In the case of films that are crystallized after a thermal treatment at 450 °C or higher, the presence of some amorphous content cannot still be excluded. It has been shown previously that when films are prepared by the soft chemical synthesis method, they contain amorphous content even when relatively high annealing temperatures are used [61]. The XRD patterns of pristine, cobalt- and nickel-containing TiO₂ films on SiO₂/Si(100) substrate annealed at 450 and 550 °C during one hour contained a weak reflex at 25.3°. The obtained peaks are attributed to the anatase phase of titania. The reflex at 25.3° became stronger and the anatase crystallites grew when the film was annealed at 650 °C. The anatase phase dominates in the films annealed below 750 °C in cobalt- and nickel-containing titania on SiO₂/Si(100) substrate. At and above 750 °C the rutile phase dominates. A noticeable amount of rutile phase appeared in the pristine titania XRD spectrum when the film was annealed at 850 °C. This indicates that cobalt and nickel addition lowers anatase to the rutile phase transition temperature. Nickel-containing titania on HF-etched Si(100) substrate demonstrated different temperature for the anatase-to-rutile phase transition as compared to nickel containing titania on SiO₂/Si(100) substrate. It was found that the anatase phase dominated in the films that had been annealed below 900 °C, at higher temperatures rutile was the dominant phase.

Additionally to different phase transition temperature, nickel-containing titania films on the SiO₂/Si(100) substrate demonstrated also stronger peaks and larger XRD peak areas as compared to the ones prepared on HF-etched Si(100) substrate, Figure 15. This indicates that nickel-containing titania films on the

SiO₂/Si(100) substrate were more crystalline than on the HF-etched Si(100) substrate.

We attribute these effects to be due to the different substrate, since everything else in our preparation protocol was the same. Although the influence of the annealing temperature on the properties of sol-gel films prepared comparably on SiO₂/Si(100) (i.e. with native oxide layer) and HF-etched Si(100) (i.e. without native oxide layer) substrate are interesting, no respective investigation has to our best knowledge been reported for titania yet.

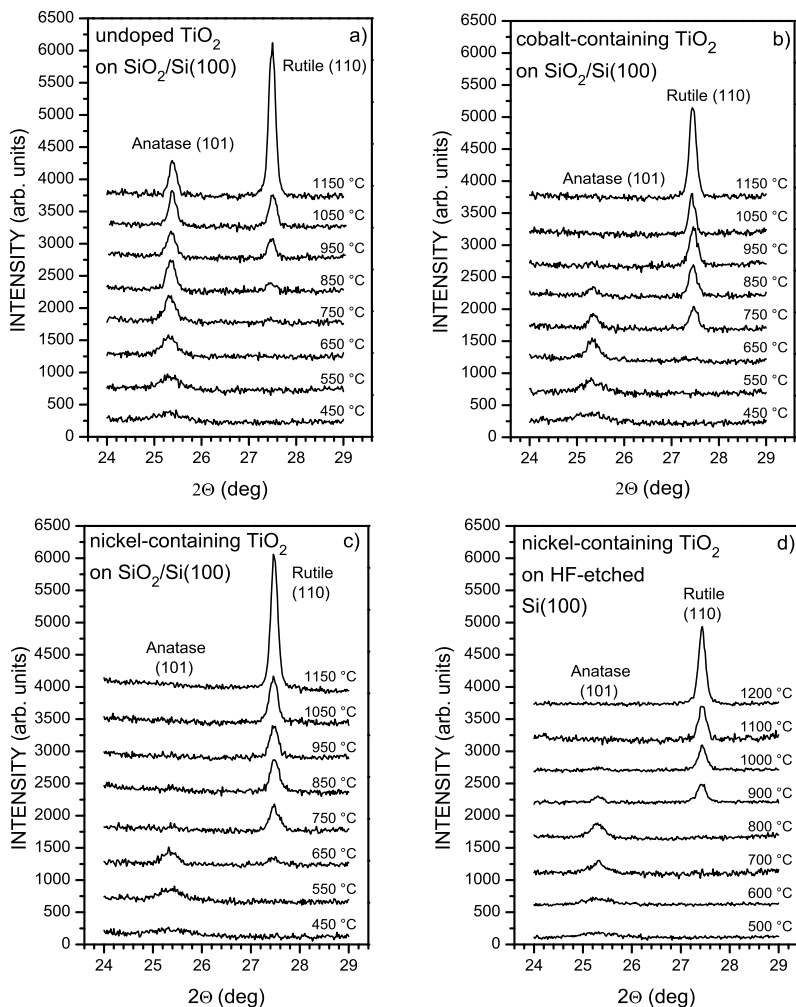


Figure 15. XRD patterns of sol-gel prepared undoped, cobalt- and nickel-containing TiO₂ films on SiO₂/Si(100) substrate (a, b, c) and nickel containing TiO₂ films on HF-etched Si(100) substrate (d) after thermal treatment at different temperatures.

However, Chen *et al.* [62] studied the influence of substrates on the characteristics of sol-gel prepared $\text{Bi}_2\text{VO}_{5.5}$ thin films. In these films sharper and stronger XRD peaks also in the case of $\text{SiO}_2/\text{Si}(100)$ substrate were observed as compared to the case of $\text{Si}(100)$ substrate. In this work better crystallinity of $\text{Bi}_2\text{VO}_{5.5}$ thin films in the case of $\text{SiO}_2/\text{Si}(100)$ substrate was explained by the presence of an SiO_2 buffer layer, which decreases the mismatch of lattice constant between the film and a Si monocystal [62]. In the case of nickel-containing TiO_2 we can speculate about a similar reason, but the mechanism of substrate influence clearly needs further investigations.

In Figure 16 (a), the calculated anatase and rutile crystallite mean sizes of undoped, cobalt- and nickel-containing titania films on $\text{SiO}_2/\text{Si}(100)$ substrate are demonstrated. Undoped, cobalt- and nickel-containing titania films composed of a nanocrystalline anatase when annealing temperature below $700\text{ }^\circ\text{C}$ were used. Although, at fixed temperatures anatase crystallites were larger in the case of cobalt-containing titania films than pristine or nickel-containing titania films. Thus, the cobalt addition predisposed the crystallization of titania. An increase of the annealing temperature led gradually to the formation of larger crystallites in the case of all films. Rutile, the phase of which dominated in cobalt- and nickel-containing titania films annealed above $750\text{ }^\circ\text{C}$, formed crystallites of about 40 to 60 nm in mean size, depending on the annealing temperature. Pristine titania contained similar size rutile crystallites when annealed above $900\text{ }^\circ\text{C}$. The further increase of the annealing temperature above $1100\text{ }^\circ\text{C}$ led to the formation of even larger crystallites in films (larger than 64 nm).

In Figure 16 (b), the calculated anatase and rutile crystallite mean sizes of nickel-containing titania films on $\text{SiO}_2/\text{Si}(100)$ and HF-etched $\text{Si}(100)$ substrates are compared. Both kinds of films contained a nanocrystalline anatase when the annealing temperature below $700\text{ }^\circ\text{C}$ was used; however, anatase crystallites were larger in the films prepared on $\text{SiO}_2/\text{Si}(100)$ substrate at a fixed temperature. Rutile, the phase of which dominated in both films annealed above $850\text{ }^\circ\text{C}$, formed crystallites of about the same size on both substrates at a fixed temperature. The formation of larger anatase crystallites on $\text{SiO}_2/\text{Si}(100)$ substrate at a fixed temperature is due to the native SiO_2 interlayer, which induces crystallization. In the case of HF-etched $\text{Si}(100)$ substrate a rather thick interlayer is formed when films are annealed at relatively high temperatures (around $800\text{ }^\circ\text{C}$). Our cross-sectional EDX measurements also demonstrated such an effect: an observable (more than 20 nm thick) interface formed between the films and substrate when they were annealed at $850\text{ }^\circ\text{C}$ (in the case of nickel-containing titania on HF-etched $\text{SiO}_2/\text{Si}(100)$ at $900\text{ }^\circ\text{C}$) [Paper IV].

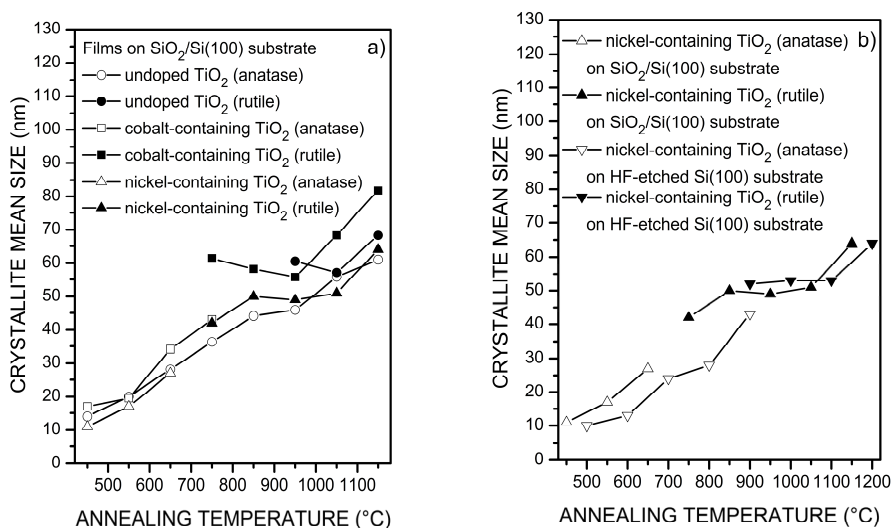


Figure 16. (a) The calculated crystallite mean sizes of undoped, cobalt- and nickel-containing titania films on SiO₂/Si(100) substrate after a thermal treatment at different temperatures. (b) The calculated crystallite mean sizes of nickel-containing titania films on SiO₂/Si(100) substrate and HF-etched Si(100) substrate after a thermal treatment at different temperatures. The lines are but eye guides.

The thicknesses of the pristine, cobalt- and nickel-containing titania films prepared on SiO₂/Si(100) substrate were determined from XRR measurements. Since XRR is sensitive to the surface roughness, more precise values could only be measured for the films annealed at lower temperatures (these films had small RMS roughness). Since all the films were spin-coated in the same regime and the organic ingredients were removed from the films during the thermal treatment, the thickness of the films annealed at 450, 550 and 650 °C (all in anatase phase) were evaluated to be similar. From XRR measurements we derived that the undoped, cobalt- and nickel-containing TiO₂ films annealed at 550 °C were about 70 nm thick. Such values correlated well with the values observed from SEM images.

In addition to XRD, the Raman spectroscopy was used to analyse the phase composition of undoped, cobalt- and nickel-containing TiO₂ films prepared on SiO₂/Si(100) substrate and nickel-containing TiO₂ films prepared on HF-etched Si(100) substrate. The results of Raman spectroscopy were generally in good accordance with XRD measurement. In addition to the crystal phases identified from XRD measurements (TiO₂ anatase and/or rutile), CoTiO₃ and NiTiO₃ bands also appeared in the Raman spectra of cobalt- and nickel-containing titania films. When the annealing temperature was increased, CoTiO₃ band at 696 cm⁻¹ and NiTiO₃ band at 705 cm⁻¹ strengthened and other bands related to CoTiO₃ and NiTiO₃ appeared. Undoped, cobalt- and nickel-containing titania films on SiO₂/Si(100) substrate annealed at 950 °C and nickel-containing titania

films on HF-etched Si(100) substrate annealed at 1000 °C are demonstrated in Figure 17A. In the Raman spectra bands related to TiO₂ (anatase and/or rutile) are observed in case of all films. In the case of cobalt- and nickel-containing titania films on SiO₂/Si(100) substrate CoTiO₃ and NiTiO₃ bands are observed. A weak NiTiO₃ band at 705 cm⁻¹ is observed in the Raman spectra of a nickel-containing titania film on HF-etched Si(100) substrate. The absence of CoTiO₃ and NiTiO₃ phases in XRD diffraction patterns can be explained by the limited sensitivity of our XRD setup, which did not allow us to detect any small amount of these phases. It should also be added that in the Raman spectra no bands related to NiO, CoO or Co₃O₄ were observed.

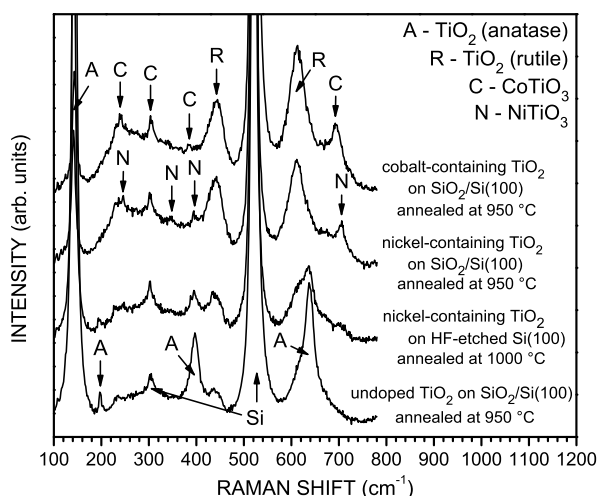


Figure 17A. The Raman spectra of the undoped, cobalt- and nickel-containing TiO₂ films prepared on SiO₂/Si(100) substrate and annealed at 950 °C. Also, the Raman spectrum of nickel- containing titania on HF-etched Si(100) substrate annealed at 1000 °C is demonstrated. Capital letters demonstrate the positions of TiO₂ anatase (A), TiO₂ rutile (R), CoTiO₃ (C) or NiTiO₃ (N) bands. Si(100) substrate bands are marked with Si and arrows.

The EDX and SEM images were recorded with a purpose to investigate the cobalt and nickel segregation and additionally the surface morphology. For analyses, EDX and SEM images of the cobalt- and nickel-containing TiO₂ films, prepared on SiO₂/Si(100) substrate annealed at 550, 850 and 950 °C, were measured. The Co and Ni EDX images are based on the Co L_{α1, β1} and Ni L_{α1, β1} fluorescence. Additionally, Si K_α fluorescence was detected. Note that the EDX is a less surface-sensitive technique, the depth of investigations depends strongly on the primary electron beam energy. To obtain a better lateral and depth resolution in EDX measurements, a low primary-electron beam energy was applied. However, usually in investigations electron beam energy

corresponding to 15-20 kV accelerating voltage is used, but the excited volume by the electron beam at this energy would be enormous as compared to the thickness and the structure features of films.

The SEM images were in good accordance with AFM images. The increase of the annealing temperature caused a formation of larger grains. It was found that the gaps between crystallites got larger when the annealing temperature was increased.

Our EDX measurements demonstrated that the annealing of cobalt- (or nickel) containing films causes a formation of regions with increased Ni and Co concentrations: strong Co $L_{\alpha 1, \beta 1}$ (demonstrated in Figure 17B) or Ni $L_{\alpha 1, \beta 1}$ fluorescence (demonstrated in Paper IV) was detected from certain areas. In addition, weak Co $L_{\alpha 1, \beta 1}$ (or Ni $L_{\alpha 1, \beta 1}$) fluorescence was measured all over the sample. When the intensity of Si K fluorescence was mapped from the film annealed at 950 °C (Figure 17B (b)), it was found that Si signal is mostly detected from the narrow irregular areas between the grains, confirming that Si substrate surface is revealed between the grains.

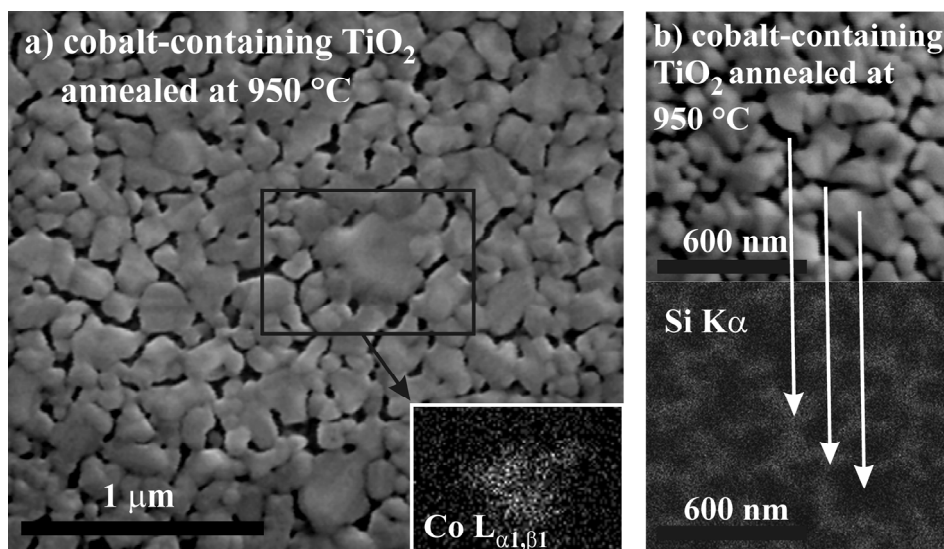


Figure 17B. The SEM and EDX images (the full image and the inset, respectively) of cobalt- containing TiO₂ films annealed at 950 °C. Solid box on SEM image (a) shows the area where the EDX image mapping for cobalt was measured. Figure (b) represents SEM image (upper part) and EDX map of Si Kα x-ray fluorescence (lower part) measured from cobalt-containing TiO₂ films annealed at 950 °C.

The Ti 2p and O 1s photoelectron spectra of undoped, cobalt- and nickel-containing TiO₂ thin films on SiO₂/Si(100) substrate annealed at 550, 750 and 950 °C are shown in Figure 18 (a-c). The respective spectra of non-heated precursor films (marked as 25 °C) are demonstrated as well. Spectral intensities are normalized to equal to Ti 2p_{3/2} peak height. Ti 2p_{3/2} and Ti 2p_{1/2} bands (right side of Figure 18 (a-c)) are located at 458.6 eV and 464.3 eV and the separation of the Ti 2p spin-orbit components was 5.7 eV. In the Ti 2p XPS spectra only the Ti⁴⁺ photoemission bands were observed, whereas no clear Ti³⁺ bands appeared. Namely, the Ti 2p_{3/2} of Ti₂O₃ should be located at about 2 eV lower binding energy than Ti 2p_{3/2} of TiO₂ [63, 64]. The XPS data of the present work are in good agreement with other TiO₂ studies [65].

In the O 1s photoelectron spectra (left side of Figure 18 (a-c)), there is a strong peak located at about 529.9 eV, which corresponds to oxygen bonded to titanium. The strong photoelectron peak was bordered with a small shoulder at 531.8 eV. The latter is related to the hydroxyl groups at the surface of films [66]. Another shoulder at 532.8 eV appeared in the spectra when the films were annealed at 750 °C and higher. This shoulder was increased in the films annealed at 950 °C and is related to silicon dioxide [67] at the top of the substrate. The band related to the silicon dioxide increased when the annealing temperature was raised. This is explained by the formation of larger grains, more substrate surface is revealed between them. Note that the precursor films prepared at room temperature did not contain cracks.

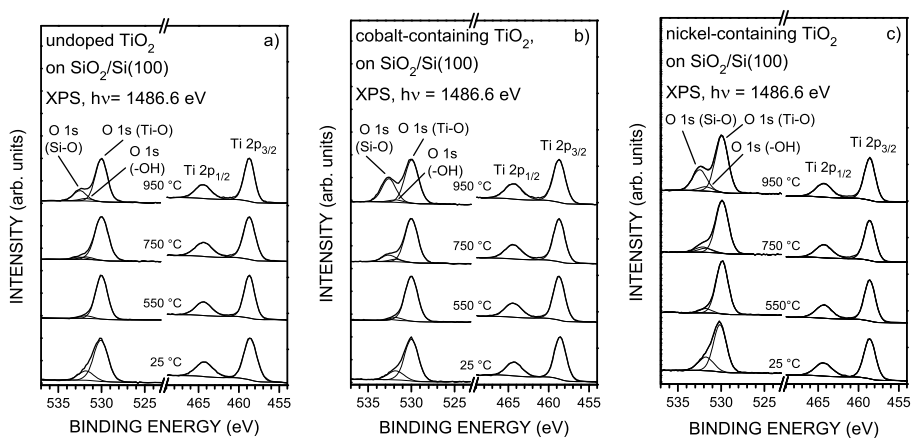


Figure 18. Ti 2p and O 1s photoelectron spectra (a) undoped TiO₂, (b) cobalt-containing TiO₂ and (c) nickel-containing TiO₂ films after a thermal treatment at different temperatures. XPS spectra of the respective non-heated aged precursor films (marked as 25 °C) are shown as well.

Figure 19 (a) displays the Co 2p photoelectron spectra of the cobalt-containing TiO₂ films annealed at different temperatures. The spectra (*i. e.*, the long scans including both the Co 2p and Ti 2p peaks) are normalized to the Ti 2p_{3/2} photoemission peak heights. The observed photoelectron lines are not typical of metallic cobalt where the spectrum should contain two separated peaks of Co 2p_{3/2} at 777.3 eV and Co 2p_{1/2} at 792.4 eV with the energy separation 15.1 eV and no satellites [68]. In our case the films, which were annealed at 550 °C, had the Co 2p_{1/2} and Co 2p_{3/2} peaks at 781 eV and 796.5 eV with the energy separation of 15.5 eV. Strong satellites were located at 786.2 eV and 802.2 eV. In the case of the films annealed at 950 °C the peaks were located at 781.2 eV and 797.1 eV (15.9 eV energy separation between the photoelectron lines). The satellites in the spectra of these samples were located at 785.9 eV and 802.8 eV.

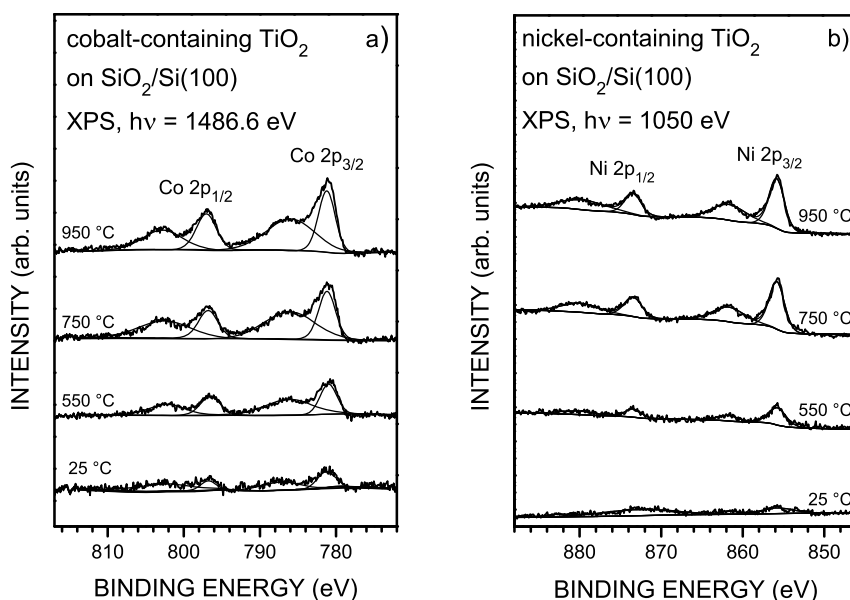


Figure 19. (a) Photoelectron spectra of Co 2p of cobalt-containing TiO₂ films on SiO₂/Si(100) annealed at different temperatures. (b) Photoelectron spectra of Ni 2p of nickel-containing TiO₂ films on SiO₂/Si(100) annealed at different temperatures. XPS spectra of non-heated aged precursor films (marked 25 °C) are displayed at the bottom.

On the basis of XPS binding energy data the presence of CoO (Co²⁺), CoTiO₃ (Co²⁺), Co₂O₃ (Co³⁺) or mixed valence Co₃O₄ (Co²⁺ and Co³⁺) in the surface can be considered, since it is hard to distinguish between these compounds by just relying on their binding energy. However, the Co 2p_{3/2} photoelectron line of CoTiO₃ spectrum is shifted to a higher binding energy as compared to CoO, Co₂O₃ and Co₃O₄ spectrum [69]. It can be distinguished between these oxides

by observing the satellites. The compounds containing high spin Co^{2+} (like CoO or CoTiO_3) have a strong satellite, but the compounds containing low spin Co^{2+} or Co^{3+} (Co_2O_3 and Co_3O_4) have weak satellites or no satellites in their photoelectron spectra [68, 69]. The presence of strong satellites in the Co 2p photoelectron spectra indicates that the Co atoms in a cobalt-containing TiO_2 film are in 2+ oxidation state, which refers to CoO or CoTiO_3 . The value of the binding energy suggests that, probably CoTiO_3 is present in the cobalt-containing titania films annealed above 650 °C. Below 650 °C probably the cobalt compounds containing high-spin Co^{2+} are present. It should be added that some Co^{2+} incorporated into titania could be considered. In that case also intense satellites are present and Co $2p_{3/2}$ binding energy is close to CoTiO_3 [69]. In conclusion, on the basis of XPS data cobalt was found to be in Co^{2+} oxidation state on the surface of the films.

Figure 19 (b) displays the Ni 2p photoelectron spectra of nickel-containing TiO_2 films annealed at 550, 750 and 950 °C. The observed photoelectron lines are not typical of a metallic nickel where the spectrum should contain two separated peaks of Ni $2p_{3/2}$ at 852.3 eV and Ni $2p_{1/2}$ at 869.7 eV with the energy separation 17.3 eV and no satellites [70, 71]. In our case, the films annealed at different temperatures had the Ni $2p_{3/2}$ photoelectron peak between 855.7 and 855.9 eV and Ni $2p_{1/2}$ photoelectron peak between 873.3 and 873.5 eV. The energy separation of these two peaks was 17.5 – 17.7 eV. Strong satellites were located between 5.7 and 6.1 eV higher binding energy than Ni $2p_{3/2}$ and between 6.3 and 6.8 eV higher binding energy than Ni $2p_{1/2}$. Such a picture is most similar to NiTiO_3 (Ni^{2+}) [72], but also another Ni compounds such as NiO may exist as well [73]. Thus, it is reasonable to conclude that in the case of the present sol-gel samples the compounds containing Ni^{2+} dominate on the surface of the annealed films. Ti 2p and Ni 2p photoelectron spectra of a nickel-containing titania film on HF-etched Si(100) substrate demonstrated also that titanium was in 4+ and Ni in 2+ oxidation state on the surface (Paper II).

The cobalt (or nickel) compounds diffusion and relative concentrations of the Co^{2+} and the Ti^{4+} (or Ni^{2+} and the Ti^{4+}) on the surface were estimated by investigating the XPS spectral bands area ratios of Ti 2p vs. Co 2p (or Ti 2p vs. Ni 2p). Firstly, the Shirley background was removed by using the CasaXPS software [54] and consecutively the band areas were measured. The Co 2p band area was taken between 772 eV and 818 eV (binding energy), the Ni 2p band area was taken between 845 eV and 890 eV (binding energy) and the Ti 2p band area between 455 eV and 469 eV.

The ratio of the Co 2p and the Ti 2p spectral band areas (integrated intensities) of the cobalt-containing TiO_2 films annealed at different temperatures are displayed in Figure 20 (a). The Figure shows that the relative amount of cobalt compounds at a thin film surface increases when the annealing temperature is increased, especially when temperatures above 650 °C are used. The same happened, when the ratio of the Ni 2p and the Ti 2p spectral band areas (integrated intensities) of nickel-containing TiO_2 films on $\text{SiO}_2/\text{Si}(100)$ annealed at different temperatures were studied (Figure 20 (b)). The XPS results are in good

agreement with the present work EDX results. Since the surface sensitivity of XPS (2-3 nm) is significantly higher than that of EDX, it can be argued that the dramatic increase in Co 2p / Ti 2p ratio (or Ni 2p / Ti 2p ratio) is a strong indication of the formation of cobalt (or nickel) compounds on top of the film and not merely in the bulk region.

Nickel-containing titania films on HF-etched Si(100) demonstrated similarly a drastic nickel compound segregation to the surface of titania during annealing, for comparison also demonstrated in Figure 20 (b). However, a rapid change appeared after annealing above 800 °C not above 650 °C, as observed in the case of titania films prepared on SiO₂/Si(100) substrate.

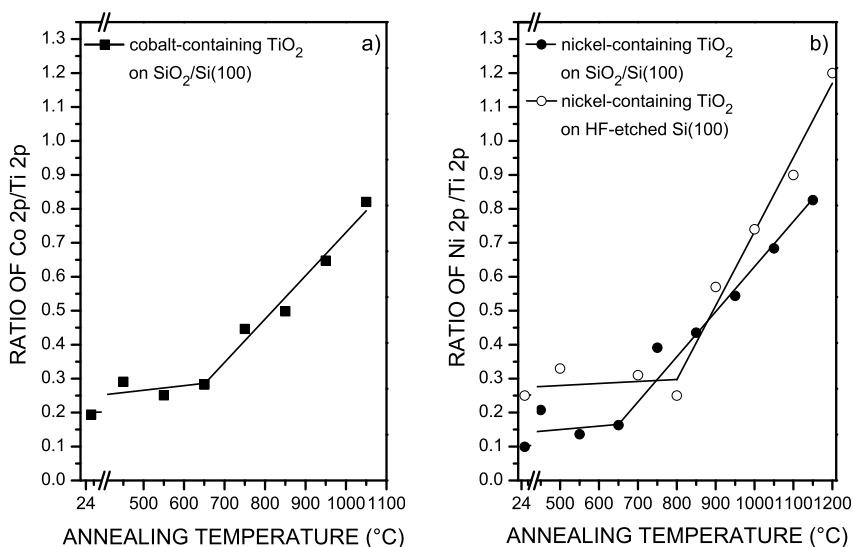


Figure 20. (a) The XPS intensity ratio of the Co 2p vs. Ti 2p band for the cobalt-containing TiO₂ films annealed at different temperatures on SiO₂/Si(100) substrate. (b) The XPS intensity ratio of the Ni 2p vs Ti 2p band for the nickel-containing TiO₂ films on SiO₂/Si(100) and HF etched Si(100) substrates annealed at different temperatures. The corresponding ratio for the non-heated aged precursor film (marked 25 °C) is demonstrated as well. The solid lines are but eye guides.

The difference of cobalt (and nickel) diffusion to the surface of films, annealed at different temperature, is in good correlation with anatase-to-rutile phase transition. The cobalt- and nickel-containing titania films on SiO₂/Si(100), composed of rutile when annealed at and above 750 °C. The nickel-containing titania films on HF-etched Si(100), composed of rutile, when annealed at and above 800 °C. It can be argued that the reason for this behaviour is the different cobalt (or nickel) incorporation to anatase and rutile. It is in good agreement

with literature, where it has been demonstrated that the amount of cobalt that replaces titanium in titania lattice depends on the TiO_2 crystal structure [14, 18].

The XAS spectra of the Ti 2p edge, measured from pristine and cobalt-containing TiO_2 films prepared on $\text{SiO}_2/\text{Si}(100)$ substrate after thermal treatment at different temperatures, are shown in Figure 21 (a). The XAS spectra of the Ti 2p edge measured from the nickel-containing TiO_2 films prepared on $\text{SiO}_2/\text{Si}(100)$ and, comparably, on the HF-etched $\text{Si}(100)$ substrate after thermal treatment at different temperatures, are shown in Figure 21 (b). The respective spectra of non-heated aged precursor films (marked as 25 °C) are shown as well. The XAS spectra consist of four main features (B, C, D, E), which arise from the spin-orbit splitting of Ti 2p level and crystal field splitting of Ti 3d levels. The peaks B and D (C and E) have previously [74] been assigned to the t_{2g} (e_g) components of the octahedral crystal field split 3d orbital in one electron picture. The asymmetry of the peak C (e_g) is due to the distortion of Ti^{4+} octahedron [75]. The pre-peaks A_1 and A_2 have a triplet character and are the crystal field split components of a minor (pre-) peak that is present already in full spherical symmetry and has been interpreted in the multiplet approach including j-j coupling considerations [76]. This complicated structure of Ti 2p XAS spectra is a fingerprint of Ti^{4+} octahedral co-ordinated by oxygen atoms, which is the case of TiO_2 . The Ti 2p XAS spectra measured from annealed pristine, cobalt- and nickel- containing titania films on $\text{SiO}_2/\text{Si}(100)$ substrate and nickel-containing titania on HF-etched $\text{Si}(100)$ substrates (Figure 21) were in good accordance to XAS spectra of TiO_2 . Thus, it was concluded that on the surface and inside the film titanium is in the same Ti^{4+} oxidation state in the case of all films.

Ti 2p XAS spectra also carry out the basic fingerprint of the bulk material crystal structure: in the case of anatase the intensity of the peak C_1 is stronger than the peak C_2 , while in the case of rutile the intensity of C_2 is stronger than C_1 [74]. The spectral structure of the undoped TiO_2 films annealed at 450 - 850 °C belongs to anatase. When the pristine TiO_2 film was annealed at 1050 °C, the feature C_2 got almost as strong as C_1 , which indicates the formation of a rutile component in the film. In the cobalt-containing TiO_2 films annealed at 450 to 650 °C, the spectral peak C_1 was stronger than C_2 . This is related to the formation of anatase in the film. In the films annealed above 750 °C the spectral peak C_2 was stronger than C_1 , which shows that rutile has formed in the films. The spectral structure of the nickel-containing titania films on $\text{SiO}_2/\text{Si}(100)$ substrate, annealed at 450 to 650 °C, belongs to anatase, the above annealed ones belong to rutile. Comparably, the spectral structure of the films on HF-etched $\text{Si}(100)$ substrate annealed lower than 900 °C belongs to anatase, the above annealed ones belong to rutile. The phase transition determined from the XAS data is in good accordance with the XRD measurements.

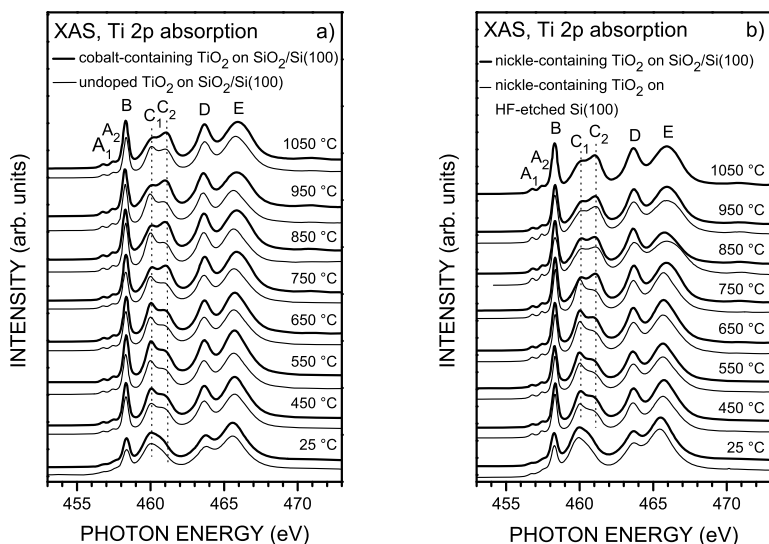


Figure 21. (a) The Ti 2p XAS spectra of cobalt-containing TiO₂ (upper thick line) and undoped TiO₂ (lower thin line) thin films on SiO₂/Si(100) after thermal treatment at different temperatures. (b) The Ti 2p XAS spectra of nickel-containing TiO₂ on SiO₂/Si(100) substrate (upper thick line) and nickel-containing TiO₂ on HF-etched Si(100) substrate (lower thin line) after thermal treatment at different temperatures. The bottom curves (marked as 25 °C) are the spectra of the aged precursor films.

XAS spectra of Co 2p of cobalt-containing TiO₂ thin films annealed at different temperatures are shown in Figure 22 (a). Co 2p XAS spectra, which are formed from the Co 2p to Co 3d dipole transitions, consist due to the spin-orbit splitting of two bands with the initial state holes at 2p_{3/2} and 2p_{1/2} levels. The Co 2p absorption edge is located above 779 eV. The structure of this edge is in good accordance with other studies of the cobalt compounds containing Co²⁺ cations, which are octahedrally coordinated by oxygen ions [77–79]. Thus, XAS spectra confirm the results from XPS measurements that cobalt is mainly in 2+ oxidation state in films.

The XAS spectra of Ni 2p region of nickel-containing TiO₂ thin films on SiO₂/Si(100) and on HF-etched Si(100), annealed at different temperatures, are shown in Figure 22 (b). Due to the spin-orbit splitting the Ni 2p XAS spectra, which are formed from the Ni 2p to Ni 3d dipole transitions, consist of two bands with the initial state holes at 2p_{3/2} and 2p_{1/2} levels. The Ni 2p absorption edge was found to be located above 852 eV. The observed Ni 2p absorption edge matches well with the other studies of nickel compounds containing Ni²⁺ cations, which are octahedrally co-ordinated by oxygen ions (like NiO, NiTiO₃) [78, 80]. Ni³⁺ cations, which are octahedrally co-ordinated by oxygen ions were not observed [80]. Thus the XAS confirmed the results of XPS measurements – in the case of films on both substrates nickel was mainly in 2+ oxidation state.

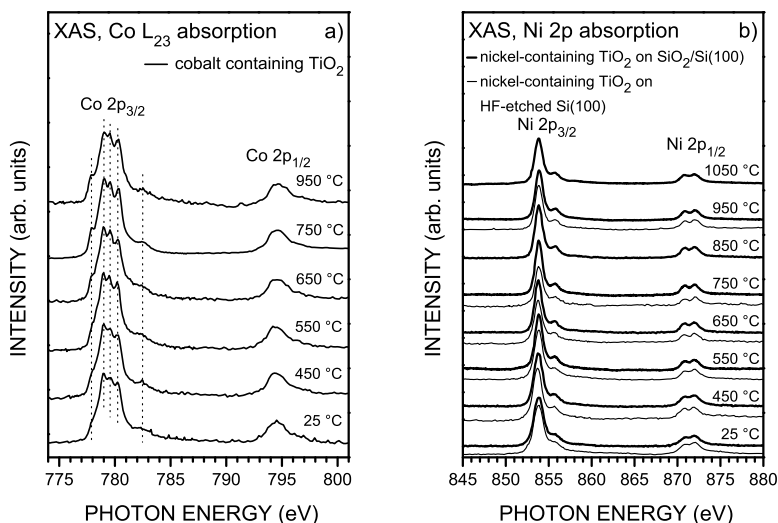


Figure 22. (a) XAS spectra of Co 2p region of cobalt-containing TiO₂ films on SiO₂/Si(100) annealed at different temperatures. (b) XAS spectra of Ni 2p region of nickel-containing TiO₂ on SiO₂/Si(100) substrate (upper thick line) and nickel-containing TiO₂ on HF-etched Si(100) substrate (lower thin line) after thermal treatment at different temperatures. The respective spectra for aged precursor films (marked 25 °C) are also demonstrated.

To evaluate the UV-Vis absorption properties of the films, the optical transmission and reflection measurements were carried out. When the absorption properties of the cobalt- and nickel-containing titania thin films are compared to the pristine titania thin films, the effect of the dopant can be seen – cobalt and nickel addition shift the titania absorption edge towards the visible spectral range. The respective spectra are demonstrated in Papers III and IV. The shift of the absorption edge is due to the cobalt (nickel) addition, however, three possible mechanisms can be responsible for that: (i) cobalt (nickel) impurity affects titania crystallite growth and lowers anatase-to-rutile phase transition temperature. Since rutile has smaller band gap than anatase, it may modify the absorption edge. (ii) The electron structure of CoTiO₃ (NiTiO₃) may affect the absorption edge. Since CoTiO₃ (NiTiO₃) has also smaller band gap than anatase TiO₂, it may modify the absorption edge. (iii) Cobalt (nickel) may substitute titanium in the titania lattice and thus additional energy levels are created in the band gap above the valence band [35].

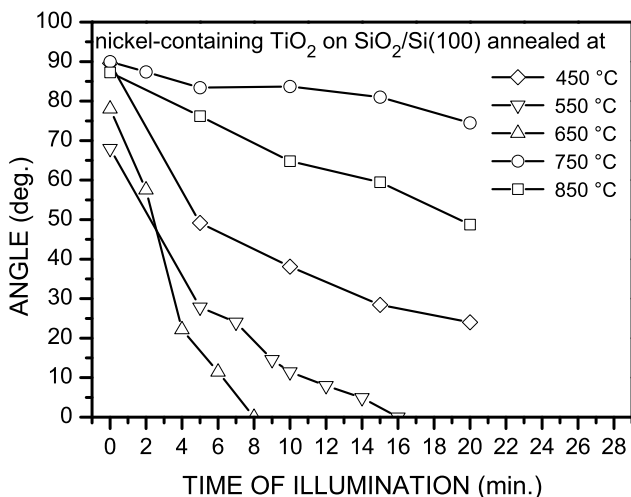


Figure 23. The change of the contact angle as a function of UV illumination time for the nickel-containing samples prepared on SiO₂/Si(100) and annealed at different temperatures. Each point in the Figure represents the time of UV illumination before one water droplet was placed on the surface and the contact angle was measured. The illumination source was an Hg-lamp (photon energy 4.89 eV). Solid lines are but eye guides.

The light-induced hydrophilicity is one of the important applications of TiO₂ films (e.g. self-cleaning windows). A mechanism of the photo-induced hydrophilicity of TiO₂ has been discussed in detail in [11].

Light-induced hydrophilicity was effectively achieved on the pristine TiO₂ surface when the films were annealed at 550, 650 and 750 °C and had crystalline anatase structures, (Figure demonstrated in Paper III). Cobalt addition did not enhance the light-induced hydrophilicity, on the contrary, the contact angle of the water droplet did not change much even after being an hour under UV illumination (respective Figure demonstrated in Paper III). Nickel-containing titania films on SiO₂/Si(100) substrate demonstrated good (surface becomes super-hydrophilic when it was less than 20 minutes under UV illumination) light-induced hydrophilic properties when annealed at 550 and 650 °C, Figure 23. Nickel-containing titania films on HF-etched Si(100) substrate also demonstrated good light-induced hydrophilic properties, although these were observed when films were annealed at 700 and 800 °C (respective Figure is demonstrated in Paper II). When comparing the results of light-induced surface hydrophilicity measurements, a tendency can be observed: good surface light-induced hydrophilic properties can be achieved when the films are composed of a well-crystallized anatase.

Conclusive results of investigations of undoped, cobalt- and nickel-containing titania films are demonstrated in Papers II–IV.

7.2. XPS and XAS study of stainless steel surface oxidation (Paper I)

Figure 24 represents the Fe 2p XPS and XAS spectra of cleaned and to a different extent oxidized Fe-19Cr-18Ni-1Al-TiC alloy and Fe 2p XAS spectra of a cleaned and oxidized Fe foil. The cleaned alloy Fe 2p XPS spectrum (Figure 24 (a), 0 L) was similar to a metallic iron, the spectrum of which consists of two separate peaks Fe 2p_{3/2} and Fe 2p_{1/2} (spin-orbit splitting) [81]. The XPS peaks related to non-oxidized iron (marked as Fe⁰ in Figure 24 (a)) were located at 707.3 eV and 720.2 eV. A cleaned Fe-19Cr-18Ni-1Al-TiC Fe 2p XAS spectrum (Figure 24 (b), 0 L) was similar to the metallic Fe foil XAS spectrum (spectrum of cleaned Fe foil in Figure 24. (b)). The absorption maxima were located at 706.5 eV and 719.3 eV in the alloy XAS spectrum and at 706.6 eV and 719.4 eV in the cleaned Fe foil XAS spectrum.

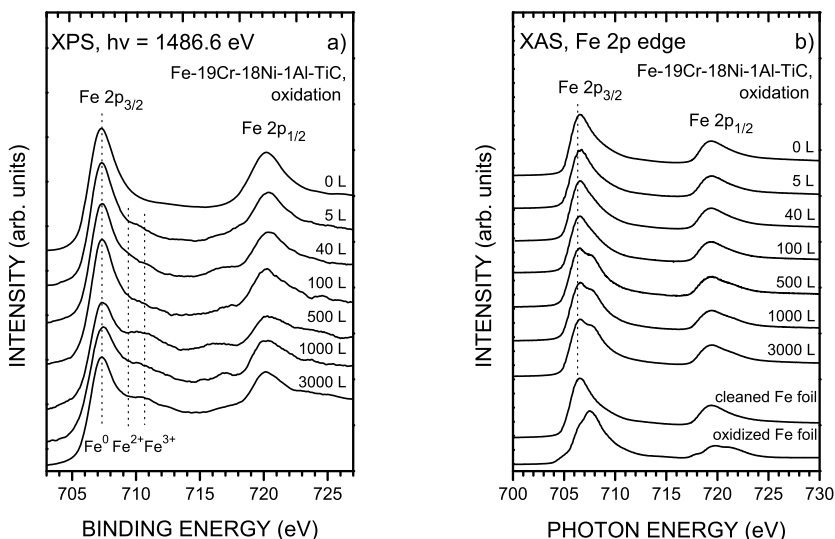


Figure 24. (a) Fe 2p XPS spectra of cleaned and to a different extent oxidized stainless steel alloy, iron oxidation states are marked as Fe⁰, Fe²⁺ and Fe³⁺; (b) Fe 2p XAS spectra of cleaned and to a different extent oxidized stainless steel alloy and the reference spectra of cleaned and oxidized Fe foil, dashed line marks the feature related to metallic iron. Oxygen exposure in Langmuirs is demonstrated besides each curve.

A change in Fe 2p XPS spectrum was detectable after 40 L of oxygen exposure, when a higher background at 709.4 eV, related to the formation of FeO (marked as Fe²⁺ in Figure 24 (a)) in the oxidation process, was observed. Another structure appeared in the XPS spectrum at 710.7 eV after 500 L of oxygen exposure. This was due to the formation of Fe₂O₃ (marked as Fe³⁺ in Figure 24

(a) in the surface layer of the alloy. Since the iron oxides were formed, the characteristic satellite peaks, related to Fe^{2+} and Fe^{3+} cations, at the higher binding energy side of the main peaks were observed as well [81]. Comparably, the XAS spectra of the alloy showed a significant change after 500 L of oxygen exposure, when a clear shoulder appeared at 707.8 eV. This shoulder was related to the iron oxides formed in the alloy surface. The observable changes in Fe 2p XAS were due to the formation of a relatively high amount of iron oxides in the surface of the alloy.

Figure 25 shows the Cr 2p XPS and XAS spectra of cleaned and to a different extent oxidized Fe-19Cr-18Ni-1Al-TiC alloy and the reference XAS spectra of a cleaned and oxidized Cr foil. Due to the spin-orbit splitting Cr 2p XPS and XAS spectra consist of two bands, $2p_{3/2}$ and $2p_{1/2}$. A cleaned alloy XPS spectrum is typical of metallic chromium (marked as Cr^0 in Figure 25 (a)) [70]. The photopeaks of Cr $2p_{3/2}$ and Cr $2p_{1/2}$ are located at 574.3 eV and 583.5 eV. XPS spectra show small changes after 5 L of oxygen exposure. The appearance of the features at 576.6 eV and 586.3 eV are related to the Cr_2O_3 formation in the alloy surface layer (marked as Cr^{3+} in Figure 25 (a)).

The Cr 2p XAS spectrum of cleaned Fe-19Cr-18Ni-1Al-TiC alloy (Figure 25 (b)) was similar to a cleaned metallic chromium spectrum [82]. The absorption structures at 575.4 eV and 584 eV were related to the x-ray absorption of metallic chromium (Figure 25 (b)). After 5 L of oxygen exposure a shoulder appeared at 576.5 eV in the Cr $2p_{3/2}$ band. This demonstrates high sensitivity of XAS to Cr oxidation in the alloy. When the oxygen exposure was increased, the shoulder in XPS and XAS spectra became stronger, having the maximum after 500 L of oxygen exposure. On a further increase of oxygen exposure the shoulders in XPS and XAS spectra slightly decreased.

The Ni 2p XAS and XPS spectra of cleaned and to a different extent oxidized Fe-19Cr-18Ni-1Al-TiC are demonstrated in Paper I. For reference, an XAS spectrum of Ni 2p of a cleaned Ni foil was measured. Before oxidation the Fe-19Cr-18Ni-1Al-TiC Ni 2p XPS spectrum consisted of two separate peaks Ni $2p_{3/2}$ and Ni $2p_{1/2}$ (due to the spin-orbit splitting), which were separated by 17.2 eV. Also, weak broad structures on the higher binding energy side of Ni 2p peaks were observed. This is typical of metallic nickel. After oxidation Fe-19Cr-18Ni-1Al-TiC XPS spectra had the same structure as the XPS spectrum of a cleaned alloy. In the cleaned Fe-19Cr-18Ni-1Al-TiC XAS spectrum two spin-orbit-split components were also observed. The Ni 2p XAS spectra of a cleaned and oxidized alloy had the same structure as the spectrum measured from a cleaned Ni foil. This confirms that nickel does not oxidize.

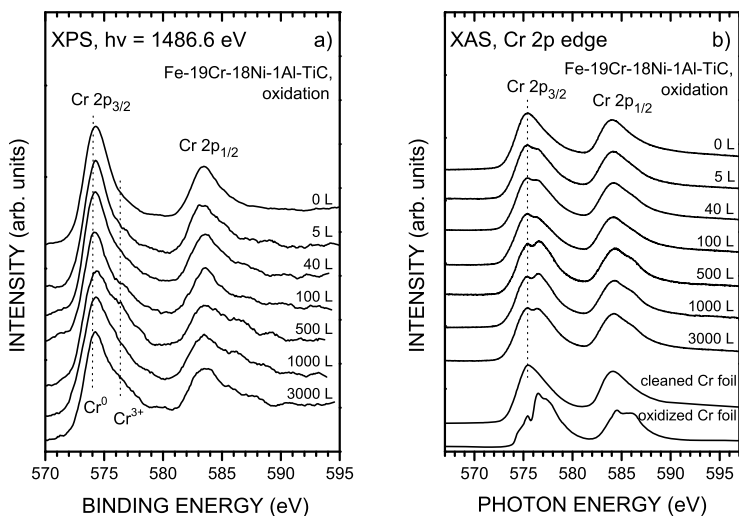


Figure 25. (a) Cr 2p XPS spectra of cleaned and to a different extent oxidized stainless steel alloy where chromium oxidation states are marked as Cr^0 and Cr^{3+} ; (b) Cr 2p XAS spectra of cleaned and to a different extent oxidized stainless steel alloy and reference spectra of cleaned and oxidized Cr foil. Dashed line marks the feature related to metallic chromium.

For a better understanding how titanium acted as an additive, the XPS and XAS spectra of Ti 2p were measured from cleaned and to a different extent oxidized Fe-19Cr-18Ni-1Al-TiC (Figure 26). Due to Ti 2p spin-orbit coupling, two bands were observed in XPS and XAS spectra, Ti $2p_{3/2}$ and Ti $2p_{1/2}$. The XPS spectra of a cleaned and oxidized sample had the same structure and no new features were monitored during the oxidation. However, the Ti $2p_{3/2}$ photoline was located at 454.9 eV. This value is typical on the formation of TiC [83].

TiC in the sample was identified from Ti 2p XAS spectra, the observed structure of this edge (Figure 26 (b)) fits well with the respective XAS structure for TiC from literature [84]. The XAS spectra did not show any change through the oxidation. This confirms that Ti stayed in the same stable compound, like it was before oxidation experiments. The XPS spectrum of C 1s (measured with the excitation energy of 400 eV) confirmed also that TiC was formed as C 1s band has the binding energy value at 281.9 eV, which is close to the respective typical value in the case of TiC [85].

The alloy Ti 2p XPS and the XAS spectra did not show any change throughout the oxidation process. This confirmed that TiC, which was identified from Ti 2p XAS and XPS spectra, did not oxidize. A XPS peak area analysis confirmed that the amount of TiC was the same throughout the oxidation.

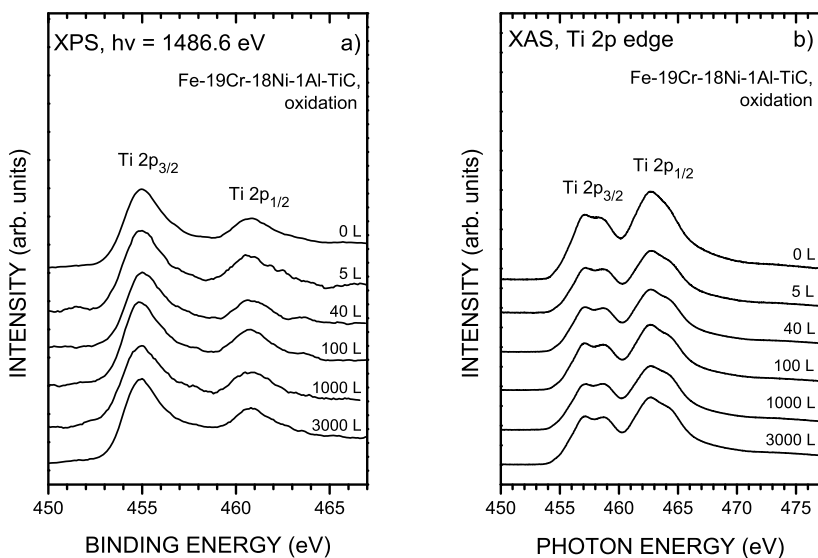


Figure 26. (a) Ti 2p XPS spectra of cleaned and to a different extent oxidized stainless steel alloy, (b) XAS spectra of Ti 2p edge of cleaned and to a different extent oxidized stainless steel alloy. Oxygen exposure in Langmuirs is demonstrated besides each curve.

The O 1s XAS spectra of 5 and 3000 L oxidized Fe-19Cr-18Ni-1Al-TiC with the spectra of oxidized Fe and Cr foils are shown in Figure 27. The spectra originate from the electronic transitions into unoccupied states with an O 2p character hybridised with metal states [86]. The interpretation of the O 1s XAS is only qualitative due to the presence of different oxides, which cause the XAS peaks overlap. O 1s XAS spectra can be divided into two parts. The first part at 527 to 533 eV corresponds to the oxygen 2p states hybridised with 3d transition metal states. The second part at 533 to 545 eV is attributed to the oxygen 2p states hybridised with metal 4s and 4p states [86].

The O 1s XAS spectrum of oxidized Fe-19Cr-18Ni-1Al-TiC alloy has similarities with the oxidized Cr foil and the oxidized Fe foil spectrum in 3d related band. As can be seen, the peak of the oxygen 2p state hybridised with a Fe 3d band is located at lower photon energies as compared to the oxygen 2p state hybridised with a Cr 3d band. This suggests that the observed structures in the alloy spectrum at 529.3 eV and 531.3 eV are related to the formed Fe_3O_4 and Cr_2O_3 , respectively, confirming that the oxide layer consists of both Fe and Cr oxides.

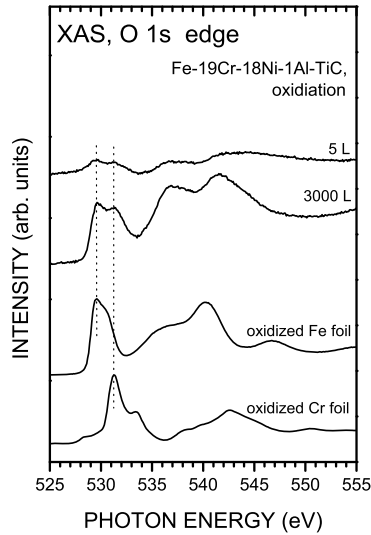


Figure 27. O 1s edge XAS spectra of 5 L and 3000 L oxidized stainless steel alloy. The measured spectra of oxidized Fe and Cr foil are also shown.

For a better understanding of the oxidation kinetics, the changes of Fe 2p, Cr 2p, Ni 2p, Ti 2p and O 1s peak areas (which are proportional to the respective changes of relative concentrations in the surface layer) were evaluated. The changes in peak areas were determined from XPS spectra measured with the excitation energy of 1486.6 eV. Fe 2p, Cr 2p, Ni 2p, Ti 2p and O 1s photopeaks were fitted by asymmetric Gaussian-Lorentzian lineshapes after subtracting a Shirley-type background.

The changes of Fe 2p (Fe^0), Cr 2p (Cr^0), Ni 2p (Ni^0), Ti 2p and O 1s peak areas (marked as Fe(met.), Cr(met.), Ni(met.), Ti(carb.), Oxygen) as a function of oxygen exposure are shown on Figure 28 (a). The changes were significant already after 5 L of oxygen exposure – as the oxygen proportion in the surface increased, the Fe^0 , Cr^0 and Ni^0 proportion decreased. The alloy surface oxidation slowed down after 100 L of oxygen exposure. After 500 L of oxygen exposure a stable protective layer in the surface of the alloy was formed. No further significant changes in the composition of the alloy surface were observed. It should be noticed that the amount of TiC stayed mostly unchanged during oxidation.

The changes of Fe 2p ($\text{Fe}^{2+}/\text{Fe}^{3+}$) and Cr 2p (Cr^{3+}) peak areas (marked as Cr(ox.) and Fe(ox.)) as a function of oxygen exposure are shown on Figure 28 (b). A rapid oxidation of Cr was observed after 5 L of oxygen exposure, a significant amount of Cr_2O_3 was formed. After 100 L of oxygen exposure the further oxidation of Cr was suppressed. Fe acted differently – at the beginning of oxidation there was only a small amount of iron oxides in the alloy surface layer. The increasing rate of the peak area related to Fe 2p ($\text{Fe}^{2+}/\text{Fe}^{3+}$) was rather

balanced as compared to the increasing rate of the peak area of Cr 2p (Cr^{3+}) (Figure 28 (b)). The peak area of Fe 2p ($\text{Fe}^{2+}/\text{Fe}^{3+}$) increased up to oxygen exposure 500 L and after that stayed stable.

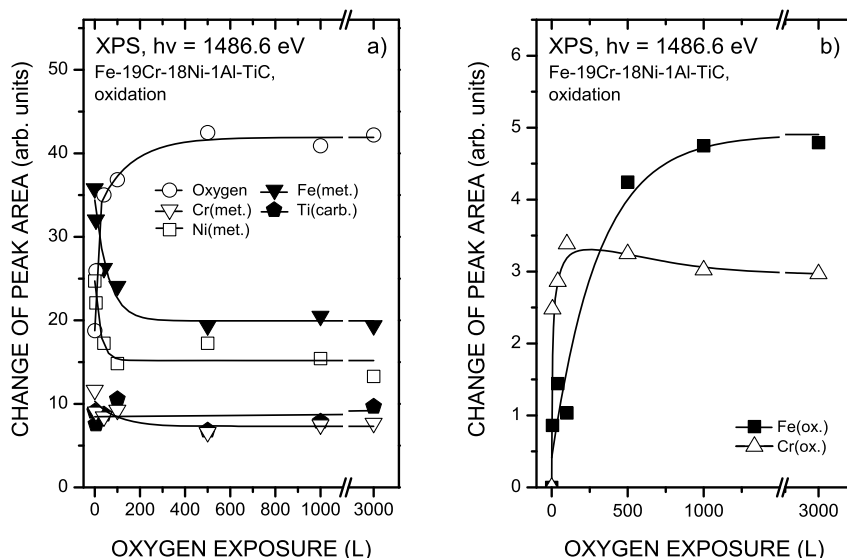


Figure 28. (a) changes of Fe 2p (Fe^0), Cr 2p (Cr^0), Ni 2p (Ni^0), Ti 2p and O 1s peak areas (marked as Fe(met.), Cr(met.), Ni(met.), Ti(carb.), Oxygen) as a function of oxygen exposure. (b) change of Fe 2p ($\text{Fe}^{2+}/\text{Fe}^{3+}$) and Cr 2p (Cr^{3+}) peak areas (marked as Cr(ox.) and Fe(ox.)) as a function of oxygen exposure. The lines are only eye guides.

In order to examine the lower binding energy region up to 120 eV in details, XPS with the excitation energy of 400 eV was used. In Figure 29, the XPS spectra of a cleaned and to a different extent oxidized Fe-19Cr-18Ni-1Al-TiC is shown. A broad valence band structure, Fe, Cr, Ni, Ti 3p and 3s, Al 2p, Al 2s and Si 2p photolines were observed. Also, a small peak related to K 3p impurity was observed at 17.3 eV.

In Fe 3p transition (demonstrated in large scale on the right of Figure 29), a shoulder appeared at 54.1 eV after 5 L of oxygen exposure. This is related to the FeO formation during the oxidation. When a 500 L dosage of oxygen was used, the peak maximum was shifted to higher energies at 55.1 eV and was broadened. It could be explained by the formation of Fe_2O_3 besides FeO in the surface of the alloy. It was also observed that the Cr 3p peak broadened after 40 L of oxygen exposure (demonstrated in a large scale on the right of Figure 29). The appearance of the shoulder at 43.2 eV was explained by the formation of Cr_2O_3 . In the case of Ni 3p peak only a change of intensity, but no new features were observed. Neither the position nor the intensity of Ti 3p changed, which

shows that Ti stays on the surface in the same chemical state. The Al 2p photoline changed only slightly after oxidations, no major changes in the peak position were observed. This indicated that Al was in the form of Al_2O_3 even before the oxidation experiments. After cleaning, Si was in the oxidation state of Si^0 (binding energy 99 eV). When oxygen was exposed to the surface, Si got oxidized quite rapidly (binding energy 101.6 eV).

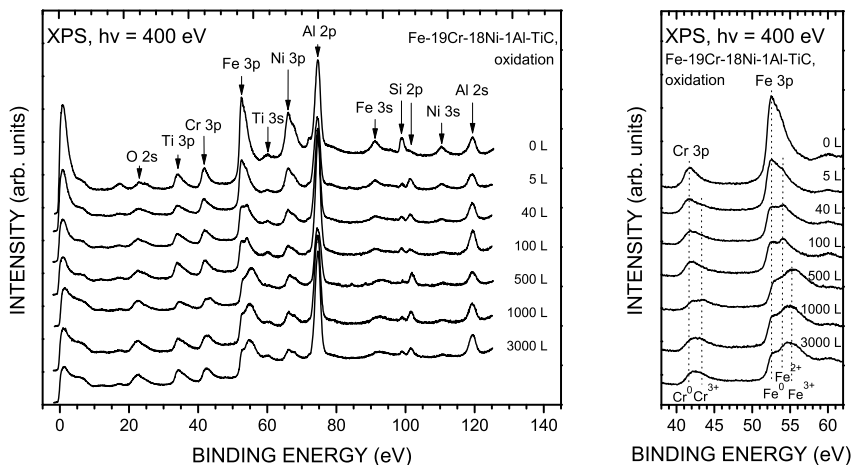


Figure 29. On the left: photoelectron spectra of cleaned and to a different extent oxidized stainless steel alloy measured by 400 eV exciting photons. On the right: Cr 2p and Fe 2p photoelectron spectra of cleaned and to a different extent oxidized stainless steel alloy measured by 400 eV exciting photons. Dotted lines demonstrate the positions of Cr^0 , Cr^{3+} , Fe^0 , Fe^{2+} and Fe^{3+} . Oxygen exposure in Langemuir is demonstrated beside each curve.

The results of the XPS and XAS study of titanium carbide-enriched austenitic stainless steel, oxidized to a different degree, are demonstrated in Paper I.

SUMMARY

In this thesis, sol-gel-prepared thin (70 nm thick) undoped, cobalt- and nickel-containing titanium(IV) oxide (TiO_2 , titania) films on $\text{SiO}_2/\text{Si}(100)$ substrate (i.e. with native oxide layer), nickel-containing titania films on HF-etched $\text{Si}(100)$ substrate (i.e. without native oxide layer) and thin chromium-rich oxide layers on the surface of stainless steel have been studied.

Titania films were studied with the aim to enhance their sunlight absorption. Effective sunlight absorption in titanium(IV) oxide is especially important in applications, such as photocatalysis, anti-fogging coatings and self-cleaning coatings. One possibility to enhance sunlight absorption in titania is to modify its electronic structure, primarily shrink the band gap. To achieve this, cobalt and nickel were added to films through the sol-gel process. In this work, the effect of annealing on the surface and the structural properties of films has been studied. Additionally, nickel-containing titania films were studied on $\text{SiO}_2/\text{Si}(100)$ - and HF-etched $\text{Si}(100)$ substrate to better understand the substrate effects on the properties of films.

In-situ in vacuum to a different degree oxidized custom-grade austenitic stainless steel was studied with a purpose to get better knowledge about the formation of chromium-rich surface oxide layer on the alloy. To enhance the inter-granular corrosion resistance of alloy, the latter was annealed to promote titanium carbide segregation to grain boundaries.

In this study, mainly surface-sensitive x-ray photoelectron spectroscopy (XPS) and x-ray absorption spectroscopy (XAS) were used to characterize pristine, cobalt- (or nickel) containing titania films and to a different degree oxidized titanium carbide-enriched austenitic stainless steel surface. In addition, such methods as atomic force microscopy (AFM), x-ray diffraction (XRD), x-ray reflection (XRR), Raman spectroscopy, energy-dispersive x-ray analysis (EDX), UV-Vis spectroscopy and hydrophilicity measurements were used.

From the studies of undoped, cobalt- and nickel-containing titania films the following conclusions were drawn. The morphological changes observed by using AFM suggested that cobalt (or nickel) addition to titania led to the formation of a rougher surface as compared to pristine titania films. On the basis of XRD it was concluded that cobalt (or nickel) addition promotes an anatase-to-rutile phase transition, which was shifted to lower annealing temperature as compared to undoped titania. It was observed that cobalt addition promotes the TiO_2 crystallite growth as compared to undoped TiO_2 . CoTiO_3 (or NiTiO_3) were observed in the Raman spectra of cobalt- (or nickel) containing titania films annealed at and above 650 °C. Below 650 °C the cobalt (or nickel) compounds containing Co^{2+} (or Ni^{2+}) were present. The EDX measurements showed that the annealing of a cobalt- (or nickel) containing TiO_2 films causes a formation of regions with increased Ni and Co concentrations. An analysis of the ratio of Ti 2p and Co 2p (or Ti 2p and Ni 2p) XPS spectral band areas showed that the concentration of cobalt (or nickel) compounds increased on the surface during annealing, especially when

temperatures above 650 °C were used. Cobalt (or nickel) in films was in 2+ and titanium in 4+ oxidation state, as confirmed by XPS and XAS measurements.

Cobalt and nickel addition induced a red shift in UV-Vis absorption spectra, which was observable when films were annealed at 750 and 950 °C. There are three possible mechanisms that can be responsible for this phenomenon: (i) cobalt (or nickel) impurity affects the growth of titania crystallite and lowers the anatase-to-rutile phase transition temperature. As rutile has a smaller band gap than anatase, it may modify the absorption edge; (ii) the formation of CoTiO_3 (or NiTiO_3) in the films, the electron structure of which affects the absorption edge of titania. Since CoTiO_3 (or NiTiO_3) has smaller band gap than TiO_2 anatase, it may modify the absorption edge. (iii) Small amount of cobalt (or nickel) substituted titanium in titania lattice and additional energy levels were created in the band gap.

Good light-induced hydrophilicity (the surface becomes super-hydrophilic when it is less than 20 minutes under UV illumination) was effectively achieved when pristine titania films were annealed at 550, 650 or 750 °C. In such case the film consisted of anatase with average crystallite sizes of 20, 28 or 36 nm, respectively. Also, nickel-containing titania films had good light-induced hydrophilic properties when annealed at 550 and 650 °C on $\text{SiO}_2/\text{Si}(100)$ substrate and 700 and 800 °C on HF-etched $\text{Si}(100)$ substrate. It was found that a well-crystallized anatase phase (with average crystallite size of 21 to 28 nm) was crucial to obtain a good light-induced hydrophilic nickel containing titania. Contrary to undoped and nickel containing titania films, cobalt-containing titania films did not have light-induced hydrophilic properties.

In addition, the effects of the substrate on the properties of nickel-containing titania films were investigated. For these investigations nickel-containing titania films were prepared on $\text{SiO}_2/\text{Si}(100)$ substrate (i.e. with native oxide layer) and on HF-etched $\text{Si}(100)$ substrate (i.e. without native oxide layer). The results demonstrated that nickel-containing titania films on $\text{SiO}_2/\text{Si}(100)$ were more uniform, had smaller RMS roughness, were better crystallized, anatase crystallites were larger and an anatase-to-rutile phase transition occurred at 150 °C lower temperature. These effects were considered to be due to the different substrate, since everything else in our preparation protocol was the same. The films prepared on both substrates demonstrated a formation of an interlayer (between films and substrates) of a couple of tens of nanometers thickness after annealing at 850 and 900 °C.

Interesting results were also obtained from the studies of titanium carbide-enriched (TiC-enriched) stainless steel surface oxidized to a different degree. When studying the alloy Fe 2p states, it was found that XPS is more sensitive to small changes in the oxide layer than XAS. Both methods were similarly sensitive concerning the study of Cr 2p, Ni 2p and Ti 2p states. Very sensitive to the formation of oxides in the alloy surface were O 1s XAS spectra, where changes were observed already after 5 L (1 L = 10^{-6} Torr·s) of oxygen exposure.

It was demonstrated that the formation of a chromium-rich passive oxide layer (i.e. protective oxide layer) on the surface of austenitic stainless steel starts already in the case of very small oxygen exposures (5 L). When the changes of Fe 2p ($\text{Fe}^{2+}/\text{Fe}^{3+}$) and Cr 2p (Cr^{3+}) photoelectronpeak areas were compared, it was found that at the beginning of surface oxidation Cr 2p (Cr^{3+}) photoelectronpeak area increased faster than Fe 2p ($\text{Fe}^{2+}/\text{Fe}^{3+}$) photoelectronpeak area. After 100 L of oxygen exposure the increase of Cr 2p (Cr^{3+}) photoelectronpeak area slowed down. When the oxygen exposure was further increased (more than 100 L), Fe 2p ($\text{Fe}^{2+}/\text{Fe}^{3+}$), the photoelectronpeak area increased. This can be explained by a greater mobility of iron cations, which move to the surface when the larger amount of oxygen is exposed to the surface. Further oxidation of the alloy is impeded after 500 L of oxygen exposure. Then a relatively stable protective oxide layer had been formed.

In the alloy nickel did not oxidize. No changes in Ni 2p states were observed, which should indicate nickel oxidation. The only change was the decrease of Ni 3p and Ni 3s photoelectronpeak areas. This indicates that the amount of Ni decreased on the surface layer.

After the alloy oxidation, titanium was in the same stable carbide form, as it was in a cleaned (not oxidized) alloy. No TiC oxidation was observed. The amount of TiC in the surface layer stayed mostly same throughout the oxidation.

It was also found that minor elements in the alloy (Al and Si) formed oxides (Al_2O_3 and SiO_x), which were also present in the passive chromium-rich surface oxide layer. However, aluminium was mostly in an oxidic form already before the alloy surface oxidation. Si oxidized when a small amount of oxygen was exposed to the surface.

SUMMARY IN ESTONIAN

“Mõningate õhukeste kiledede pinnauuringud”

Antud doktoritöös uuriti õhukesti (70 nm paksuseid) sool-geel meetodil valmistatud lisandita, koobalti ja nikli lisandiga titaan(IV)oksiid (TiO_2) kilesid $\text{SiO}_2/\text{Si}(100)$ kasvualusel (loomuliku oksiidikihiiga monokristall), nikli lisandiga titaan(IV)oksiid kilesid vesinikfluoriidhappega (HF) söövitatud $\text{Si}(100)$ kasvualusel (ilma loomuliku oksiidikihiiga monokristall) ning õhukesti kroomirikkaid oksiidikihte austeniitse roostevaba terase pinnal.

TiO_2 kilesid uuriti eesmärgiga parandada selles materjalis päikesevalguse neeldumist. Efektiivne päikesevalguse neeldumine titaan(IV)oksiidis on eriti oluline rakendustes nagu näiteks fotokatalüüs, uduvastased pinnakatted ja isepuhastuvad pinnakatted. Üheks titaan(IV)oksiidi päikesevalguse neeldumise parandamiseks on tema elektronstruktuuri modifitseerimine, eelkõige keelutsooni laiuse vähendamine. Selle saavutamiseks lisati TiO_2 kiledetele koobaltit ja niklit, kasutades sool-geel meetodit. Töös on uuritud lõõmutustemperatuuri mõju kiledete pinnale ja struktuurile. Lisaks uuriti niklit sisaldavaid TiO_2 kilesid $\text{SiO}_2/\text{Si}(100)$ ja HF söövitatud $\text{Si}(100)$ kasvualusel, et paremini mõista kasvualuse mõju kile omadustele.

In-situ vaakumsüsteemis erineval määral oksüdeeritud spetsiaalselt valmistatud austeniitset roostevaba terast uuriti eesmärgiga, et paremini mõista kroomirikka (passiivse) oksiidikihi moodustumist sulami pinnal. Selle konkreetse austeniitse roostevaba terase teradevahelist korrosioonikindlust tõsteti lõõmutamise teel. See viis titaankarbiidi moodustumiseni teradevahelistele piirpindadele.

Antud doktoritöös kasutati põhiliselt röntgenfotoelektron-spektroskoopia ja röntgenneeldumisspektroskoopia meetodeid, et karakteriseerida lisandita, koobalti (või nikli) lisandiga titaan(IV)oksiid kilesid ja pinna erineval määral oksüdeerimisega saadud kroomirikast pinnaoksiidi titaankarbiidiga rikastatud roostevabal terasel. Lisaks kasutati järgmiseid meetodikaid: aatomjõumikroskoopia, röntgendifraktsioon, röntgenpeegeldus, Raman spektroskoopia, energiadispersiivne röntgenanalüüs, UV-Vis spektroskoopia ja hüdrofiilsuse mõõtmine.

Lisandita ja koobalti (või nikli) lisandiga TiO_2 kiledete uuringutest saab välja tuua järgmisi tulemusi. Pinnakareduse uuringud aatomjõumikroskoobiaga näitasid, et koobalti (või nikli) lisand viis karedama pinna moodustumiseni, võrreldes lisandita titaan(IV)oksiid kiledetega. Röntgendifraktsiooni põhjal saab väita, et koobalti (või nikli) lisand soodustab anataasi üleminekut rutiiliks, anataas-rutiil faasisiire oli nihutatud madalamale lõõmurustemperatuurile võrreldes lisandita titaan(IV)oksiid kiledetega. Koobalti lisand soodustas kristalliitide kasvu võrreldes lisandita TiO_2 kilega. Lisandiga kiledes, mis olid lõõmutatud $650\text{ }^\circ\text{C}$ juures ja kõrgemal temperatuuril, tuvastati CoTiO_3 (või NiTiO_3), kasutades Raman spektroskoopiat. Kiled, mis olid lõõmutatud madalamal temperatuuril kui $650\text{ }^\circ\text{C}$, sisaldasid Co^{2+} (või Ni^{2+}) ühendeid. Energiadispersiivne röntgenanalüüs näitas, et koobalti (või nikli) lisandiga kiledete lõõmutamine viib

piirkondade moodustumiseni, kus on suurenenud koobalti (või nikli) kontsentratsioon. Ti 2p ja Co 2p (või Ti 2p ja Ni 2p) röntgenfotoelektronpiikide pindalade suhte analüüs näitas, et koobalti (või nikli) ühendite kontsentratsioon suurenes pinnakihis lõõmutamise käigus, eriti kui kasutati lõõmutustemperatuure üle 650 °C. Röntgenfotoelektron-spektroskoopia ja röntgenneeldumisspektroskoopia mõõtmised näitasid, et koobalt (või nikkel) olid kiledes 2+ oksüdatsiooniastmes ning titaan 4+ oksüdatsiooniastmes.

Koobalti (või nikli) lisand põhjustas UV-Vis neeldumisspektrites punanihke, see oli märgatav, kui kiled olid lõõmutatud temperatuuridel 750 ja 950 °C. Sellel efektil võib olla kolm põhjust: (i) koobalti (või nikli) lisand mõjutas titaan(IV)oksiidi kristalliitide kasvu ja viis anataas-rutiil faasisiirde madalamale temperatuurile. Kuna rutiil on väiksema keelutsooni laiusega kui anataas, siis muutis see materjali neeldumisaärt, (ii) CoTiO_3 (või NiTiO_3) teke kiledes, mille elektronstruktuur mõjutas valguse neeldumist titaan(IV)oksiidis. Nimelt on CoTiO_3 -l (või NiTiO_3 -l) väiksem keelutsooni laius kui TiO_2 anataasil. (iii) Väike kogus koobaltit (või niklit) vahetab välja titaani TiO_2 võres ja tekkivad lisandinivood keelutsooni.

Head valguse poolt indutseeritud hüdrofiilsed omadused (pind muutub super-hüdrofiilseks olles UV valguse all vähem kui 20 minutit) olid lisandita TiO_2 kiledel, mis olid lõõmutatud 550, 650 või 750 °C juures. Sellisel juhul koosnes kile anataasi kristalliitidest keskmiste diameetritega 20, 28 või 36 nm. Samuti head valguse poolt indutseeritud hüdrofiilsed omadused olid nikli lisandiga TiO_2 kiledel $\text{SiO}_2/\text{Si}(100)$ kasvualustel, mis olid lõõmutatud 550 ja 650 °C juures ning HF-iga söövitatud $\text{Si}(100)$ kasvualustel, mis olid lõõmutatud 700 ja 800 °C juures. Leiti, et head valguse poolt indutseeritud hüdrofiilsed omadused olid nikli lisandiga titaan(IV)oksiidi kiledel, kui need koosnesid anataasist, mille keskmine kristalliidi suurus oli 21 kuni 28 nm. Vastupidiselt lisandita ja nikli lisandiga TiO_2 kiledele ei olnud häid valguse poolt indutseeritud hüdrofiilseid omadusi koobalti lisandiga kiledel.

Lisaks uuriti kasvualuse mõju nikli lisandiga titaan(IV)oksiidi kilede omadustele. Nendeks uuringuteks valmistati niklit sisaldavad titaan(IV)oksiidi kiled $\text{SiO}_2/\text{Si}(100)$ (loomuliku oksiidikihiga) ja HF söövitatud $\text{Si}(100)$ (ilma loomuliku oksiidikihita) kasvualustele. Tulemused näitasid, et nikli lisandiga titaani(IV)oksiidi kiled, mis olid valmistatud $\text{SiO}_2/\text{Si}(100)$ kasvualusele, olid palju ühtlasemad – neil oli väiksem pinnakaredus, nad olid rohkem kristalliseerunud, anataasi kristalliidid olid suuremad ja anataas-rutiil faasisiire oli 150 °C madalamal temperatuuril. Need efektid omistati erinevustele kasvualustes, kuna kõik muu eksperimendi protokollis oli sama. Kilede puhul, mis olid valmistatud mõlemat tüüpi kasvualusele, mõõdeti mõnekümne nanomeetri paksune vahekiht (kile ja kasvualuse vahel) alles pärast 850 and 900 °C juures lõõmutamist.

Huvitavaid tulemusi saadi ka titaankarbiidiga (TiC) rikastatud austeniitse roostevaba terase erineval määral oksüdeeritud pinna uuringutest. Kui uuriti sulami Fe 2p seisundeid, siis leiti, et röntgenfotoelektron-spektroskoopia on tundlikum väiksematele muutustele oksiidikihis, kui röntgenneeldumisspektroskoopia. Mõlemad meetodid näitasid sarnast tundlikkust, kui uuriti Ni, Cr ja Ti

2p seisundeid. Väga suurt tundlikkust oksiidide moodustumise suhtes sulami pinnakihis näitas O 1s ääre röntgenneeldumisspektroskoopia, kus juba peale 5 L ($1 \text{ L} = 10^{-6} \text{ Torr}\cdot\text{s}$) hapniku ekspositsiooni olid muutused jälgitavad.

Näidati, et passiivse kroomirikka oksiidikihi (kaitsva oksiidikihi) moodustumine austeniitse roostevaba terase pinnale algab juba sulami oksüdeerimisel väga väikese koguse hapnikuga (ekspositsioon 5 L). Kui võrreldi muutusi Fe 2p ($\text{Fe}^{2+}/\text{Fe}^{3+}$) ja Cr 2p (Cr^{3+}) röntgenfotoelektronpiikide pindalades, leiti, et pinna oksüdeerumise alguses suurenes Cr 2p (Cr^{3+}) röntgenfotoelektronjoonte pindala kiiremini kui Fe 2p ($\text{Fe}^{2+}/\text{Fe}^{3+}$) röntgenfotoelektronpiigi pindala. Peale 100 L hapniku ekspositsiooni pidurdus Cr 2p (Cr^{3+}) röntgenfotoelektronpiigi pindala juurdekasv. Pärast edasist hapniku ekspositsiooni suurendamist (üle 100 L), Fe 2p ($\text{Fe}^{2+}/\text{Fe}^{3+}$) röntgenfotoelektronpiigi pindala jätkas kasvamist. See oli seletatav raua kationide suurema mobiilsusega, mis liikusid pinnale, kui suurem kogus hapnikku oli pinnale juhitud. Sulami edasine oksüdeerumine pidurdus pärast seda, kui oli kasutatud hapniku ekspositsiooni 500 L. Siis oli moodustunud suhteliselt stabiilne kaitsev oksiidikiht.

Sulamis nikkel ei oksüdeerunud. Ni 2p seisundites muutusi, mis viitaksid nikli oksüdeerumisele ei tuvastatud. Ainsaks muutuseks oli Ni 3p ja Ni 3s röntgenfotoelektronpiikide pindala vähenemine. See viitas nikli koguse vähenemisele sulami pinnal.

Peale sulami oksüdeerumist oli titaan samas karbiidses olekus, nagu puhastatud (oksüdeerimata) sulamis. Titaankarbiid ei oksüdeerunud. Titaankarbiidi kogus pinnakihis ei muutunud sulami oksüdeerumise käigus.

Lisaks leiti, et alumiinium ja räni, mida oli sulamis väikeses koguses, moodustasid okside (Al_2O_3 ja SiO_x), mis olid samuti olemas passiivses kroomirikas pinnaoksiidikihis. Tuleb lisada, et alumiinium oli enamjaolt oksiidises olekus juba enne sulami oksüdeerimist. Räni oksüdeerus juba väikese koguse hapniku kasutamisel.

ACKNOWLEDGEMENT

Above all I would like to express my greatest gratitude to my supervisors Vambola Kisand and Professor Ergo Nõmmiste for their guidance and support during my PhD studies. I would like to acknowledge Mika Hirsimäki and Professor Mika Valden for their guidance and fruitful discussions during my stay at Tampere University of Technology.

I would like to express my gratitude to my colleagues and co-workers at the Laboratory of X-Ray Spectroscopy (University of Tartu, Institute of Physics), particularly to Arvo Kikas and Urmas Joost, also, to Ivar Kuusik, Tanel Käämbre, Agu Saar, Rein Ruus, Leonard Matisen. My thanks go to my colleagues at the Surface Science Laboratory (Tampere University of Technology) Petri Jussila, Marko Ahonen, Leena Kannanen, Niina Jokkinen and Tero Liimainen. I would also like to thank Ilmar Kink from Estonian Nanotechnology Competence Center. I am grateful to my colleagues at the Laboratory of Thin-Film Technology (University of Tartu, Institute of Physics) especially Aivar Tarre, Arnold Rosental, Ahti Niilisk, Professor Jaan Aarik and Professor Väino Sammelselg for their guidance and support, and Hugo Mändar for his guidance with XRD and XRR measurements. I would also like to thank Arne Kasikov, Margus Marandi, Peeter Ritslaid, Jelena Asari, Alar Gerst and Ivan Netšipailo, also, Evi Vaik for language consultations.

I am grateful to the staff of MAX-laboratory, especially to Alexei Preobrajenski for the assistance and co-operation during the measurements at beamline D1011.

This work has been partially supported by graduate school „Functional materials and technologies“ receiving funding from the European Social Fund under project 1.2.0401.09-0079 in Estonia.

I acknowledge the following agencies and foundations for the financial support: Estonian Science Foundation (grants 8216, 8420, 8737 and 7615); Estonian Nanotechnology Competence Center; Estonian Ministry of Education and Research (target-financed themes SF0180058s07 and SF0180046s07); NordForsk; and European Community's Seventh Framework Programme (FP7/2007-2013) under grant agreement n^o 226716.

Finally, I would like to give my warmest thanks to my life companion Liis, my family, and friends for their help, support and interest in my work during these years.

REFERENCES

- [1] M. Keshmiri, M. Mohseni, T. Troczynski, *Appl. Catal. B Environ.* 53 (2004) 209–219.
- [2] G.K. Keima, M.J. Colgan, M.J. Brett, *Solar Energy Mater. Solar Cells* 85 (2005) 321–331.
- [3] R. Wang, K. Hashimoto, A. Fujishima, M. Chikuni, E. Kojima, A. Kitamura, M. Shimohigoshi, T. Watanabe, *Nature* 388 (1997) 431–432.
- [4] R. Wang, K. Hashimoto, A. Fujishima, M. Chikuni, E. Kojima, A. Kitamura, M. Shimohigoshi, T. Watanabe, *Adv. Mater.* 10 (1998) 135–138.
- [5] G. Eranna, B.C. Joshi, D.P. Runthala, R.P. Gupta, *Crit. Rev. Solid State Mater. Sci.* 29 (2004) 111–188.
- [6] M. Radecka, K. Zakrzewska, M. Wierzbicka, A. Gorzkowska, S. Komornicki, *Solid State Ionics* 157 (2003) 379–386.
- [7] C. Cantalini, *J. Eur. Ceram. Soc.* 24 (2004) 1421–1424.
- [8] V. Teixeira, E. Sousa, M.F. Costa, C. Nunes, L. Rosa, M.J. Carvalho, M. Collares-Pereira, E. Roman, J. Gago, *Thin Solid Films* 392 (2001) 320–326.
- [9] M.D. Bijker, J.J.J. Bastiaens, E.A. Draaisma, L.A.M. de Jong, E. Sourty, S.O. Saied, J.L. Sullivan, *Tribol. Int.* 36 (2003) 227–233.
- [10] J. Beddoes, J.G. Parr, Introduction to Stainless Steels, 3rd edition, ASM International, Materials Park, OH, 1999, pp. 7–13.
- [11] O. Carp, C.L. Huisman, A. Reller, *Prog. Solid State Chem.* 32 (2004) 33–177.
- [12] A. Pardo, M.C. Merino, A.E. Coy, F. Viejo, M. Carboneras, R. Arrabal, *Acta Materialia* 55 (2007) 2239–2251.
- [13] M. Terada, M. Saiki, I. Costa, A.F. Padilha, *J. Nucl. Mat.* 358 (2006) 40–46.
- [14] S.H. Lim, C. Ferraris, M. Schreyer, K. Shih, J.O. Leckie, T.J. White, *J. Solid State Chem.* 180 (2007) 2905–2019.
- [15] M. Subramanian, S. Vijayalakshmi, S. Venkataraj, R. Jayavel, *Thin Solid Films* 516 (2008) 3776–3782.
- [16] S.D. Sharma, D. Singh, K.K. Saini, C. Kant, V. Sharma, S.C. Jain, C.P. Sharma, *Appl. Catal. A: General* 314 (2006) 40–46.
- [17] J.C. Rawers, *Oxidation of Metals* 29 (1988) 371–389.
- [18] M. Fleischhammer, M. Panthöfer, W. Tremel, *J. Solid State Chem.* 182 (2009) 942–947.
- [19] M.A. Barakat, G. Hayes, S. Ismat Shah, *J. Nano. Nanotech.* 5 (2005) 759–765.
- [20] J. F. Watts, J. Wolstenholme, An Introduction to Surface Analysis by XPS and AES, John Wiley & Sons Ltd, Chichester, 2003, pp. 1–14.
- [21] J. Stöhr, NEXAFS spectroscopy, Springer-Verlag, Berlin, 1992, pp. 8–11, pp. 114–161.
- [22] L.M. Nikolić, L. Radonjić, V.V. Srdić, *Ceram. Int.* 31 (2005) 261–266.
- [23] P. Jussila, K. Lahtonen, M. Lampimäki, M. Hirsimäki, M. Valden, *Surf. Interface Anal.* 40 (2008) 1149–1156.
- [24] M. Lampimäki, K. Lahtonen, P. Jussila, M. Hirsimäki, M. Valden, *J. Elec. Spec. Rel. Phenom.* 154 (2007) 69–78.
- [25] R.B. King, Ed., Encyclopedia of Inorganic Chemistry, vol.8, Wiley, Chichester, 1994, pp. 4198–4199.
- [26] D.A.H. Hanaor, C.C. Sorrell, *J. Mater. Sci.* 46 (2011) 855–874.

- [27] J.R. Smyth, T.C. McCormick, Crystallographic Data for Minerals, in: T.J. Ahrens, Ed., Mineral Physics and Crystallography: A Handbook of Physical Constants, American Geophysical Union, 1995, pp. 2.
- [28] Gmelins Handbuch der Anorganischen Chemie, System Nummer 41, Chemie, Weinheim, 1951, pp. 232–251.
- [29] X. Hong, Z. Wang, W. Cai, F. Lu, J. Zhang, Y. Yang, N. Ma, Y. Liu, *Chem. Mater.* 17 (2005) 1548–1552.
- [30] Z.G. Li, S. Miyake, *Appl. Surf. Sci.* 255 (2009) 9149–9153.
- [31] R. López, R. Gómez, M.E. Llanos, *Catal. Today* 148 (2009) 103–108.
- [32] R.S. Sonawane, B.B. Kale, M.K. Dongare, *Mater. Chem. Phys.* 85 (2004) 52–57.
- [33] K.-S. Hwang, J.-H. Jeong, J.-H. Ahn, B.-H. Kim, *Ceramics International* 32 (2006) 935–937.
- [34] J. Chen, N. Yao, R. Wang, J. Zhang, *Chemical Engineering Journal* 148 (2009) 164–172.
- [35] T. Umebayashi, T. Yamaki, H. Itoh, K. Asai, *J. Phys. Chem Sol.* 63 (2002) 1909–1920.
- [36] A. Fujishima, K. Honda, *Nature* 238 (1972) 37–38.
- [37] S.N. Frank, A.J. Bard, *J. Am. Chem. Soc.* 99 (1977) 303–304.
- [38] S. Anandan, Y. Ikuma, K. Niwa, *Sol. State Phenom.* 162 (2010) 239–260.
- [39] V. Agugliaro, V. Lobbo, M. Pagliaro, G. Palmisano, L. Palmisano, Clean by light irradiation practical applications of Supported TiO₂, The Royal Society of Chemistry Publishing, UK, 2010. pp. 1–16.
- [40] S.M. Lam, J.C. Sin, A.R. Mohamed, Recent Patents on Chemical Engineering, 1 (2008) 209–219.
- [41] C.P. Dillon, Corrosion Resistance of Stainless Steels, Corrosion Technology 9, New York, N.Y., USA, 1995. pp. 3–23.
- [42] C.O.A. Olsson, D. Landolt, *Electrochim. Acta* 48 (2003) 1093–1104.
- [43] A.C. Pierre, Introduction to sol-gel processing, Kluwer Academic Publishers, Boston, 1998. pp. 2–8.
- [44] C.J. Brinker, G.W. Sherer, Sol-gel Science: The Physics and Chemistry of Sol-gel Processing, Academic Press, Boston, 1990. pp. 2–11.
- [45] Allegheny Ludlum, Technical Data Blue Sheet, Stainless Steel Type 334, ATI Allegheny Ludlum: Pittsburgh, 1999, <http://www.alleghenyludlum.com>, 2010.
- [46] G. Bunker, Introduction to XAFS, Cambridge University Press, Cambridge, UK, 2010. pp. 1–20.
- [47] J.H. Hubbell, A.H. Gimm, I. Øverbø, *J. Phys. Chem. Ref. Data* 9 (1980) 1023–1149.
- [48] D.T. Attwood, Soft X-Rays and Extreme Ultraviolet Radiation: Principles and Applications, Cambridge University Press, Cambridge, 1999. pp. 3.
- [49] S. Hüfner, Photoelectron Spectroscopy—Principles and Applications, 3rd ed. Berlin, Springer, 2003. pp. 1–27
- [50] J.A.R Samson, D.L. Ederer, Vacuum Ultraviolet Spectroscopy, Academic Press, 2000. pp. 1–21.
- [51] J. Als-Nielsen, D. McMorrow, Elements of Modern X-ray Physics, John Wiley & Sons Ltd, New York, 2001, pp. 2.
- [52] <http://www.maxlab.lu.se/beamline/max-ii/d1011/d1011.html>, 2011.
- [53] <http://www.maxlab.lu.se/beamlines/bli511/>, 2011.
- [54] N. Fairley, CasaXPS version 2.3.12, www.casaxps.com, 2000.
- [55] B.E. Warren, X-ray diffraction, Dover Publications, New York, 1990. pp. 15–16.

- [56] A. Beiser, *Concepts of Modern Physics*, sixth edition, McGraw-Hill, New York, 2003, pp. 72–75.
- [57] P. Scherrer, *Nachr. Ges. Wiss. Gott.* **26** (1918) 98–100.
- [58] D. Nečas, P. Klapetek, C. Anderson, Gwyddion version 2.19, <http://gwyddion.net/>, 2010.
- [59] P. Vitanov, Tz. Babeva, Z. Alexieva, A. Harizanova, Z. Nenova, *Vacuum* **76** (2004) 219–222.
- [60] H. Tang, K. Prasad, R. Sanjinès, P.E. Schmid, F. Lévy, *J. Appl. Phys.* **75** (1994) 2042–2047.
- [61] J.R. Ares, A. Pascual, I.J. Ferrer, C. Sánchez, *Thin Solid Films* **480–481** (2005) 477–481.
- [62] F. Chen, H.M. Deng, D.J. Huang, P.X. Yang, J.H. Chu, *J. Phys: Conf. Series* **276** (2011) 012160.
- [63] S. Hashimoto, A. Tanaka, *Surf. Interface Anal.* **34** (2002) 262–265.
- [64] M. Dhayal, S.D. Sharma, C. Kant, K.K. Saini, S.C. Jain, *Surf. Sci.* **602** (2008) 1149–1154.
- [65] R. Sanjinés, H. Tang, H. Berger, F. Gozzo, G. Margaritondo, F. Lévy, *J. Appl. Phys.* **75** (1994) 2945–2951.
- [66] J. Yu, J.C. Yu, W. Ho, Z. Jiang, *New J. Chem.*, **26** (2002) 607–613.
- [67] M.L. Miller, R.W. Linton, *Anal. Chem.* **57** (1985) 2314–2319.
- [68] B.J. Tan, K.J. Klabunde, P.M.A. Sherwood, *J. Am. Chem. Soc.* **113** (1991) 855–861.
- [69] Y. Brik, M. Kacimi, M. Ziyad, F. Bozon-Verduraz, *J. Catal.* **202** (2001) 118–128.
- [70] C.D. Wagner, W.M. Riggs, L.E. Davis, J.F. Moulder, G.E. Muilenberg (Eds.), *Handbook of x-ray photoelectron spectroscopy*, Perkin-Elmer Corporation, Eden Prairie, 1979.
- [71] F.U. Hillebrecht, J.C. Fuggle, P.A. Bennett, Z. Zolnierok, *Phys. Rev. B: Condens. Matter Mater. Phys.* **27** (1983) 2179–2193.
- [72] S.-W. Ho, C.-Y. Chu, S.-G. Chen, *J. Catal.* **178** (1998) 34–48.
- [73] D. Alders, F.C. Voogt, T. Hibma, G.A. Sawatzky, *Phys. Rev. B: Condens. Matter Mater. Phys.* **54** (1996) 7716–7719.
- [74] R. Ruus, A. Kikas, A. Saar, A. Ausmees, E. Nõmmiste, J. Aarik, A. Aidla, T. Uustare, I. Martinson, *Solid State Commun.* **104** (1997) 199–203.
- [75] F.M.F. de Groot, M.O. Figueiredo, M.J. Basto, M. Abbate, H. Petersen, J.C. Fuggle, *Phys. Chem. Miner.* **19** (1992) 140–147.
- [76] F.M.F. de Groot, J.C. Fuggle, B.T. Thole, G.A. Sawatzky, *Phys. Rev. B* **41** (1990) 928–937.
- [77] S.A. Chambers, C.M. Wang, S. Thevuthasan, T. Droubay, D.E. McCready, A.S. Lea, V. Shutthanandan, C.F. Windisch Jr., *Thin Solid Films* **418** (2002) 197–210.
- [78] G. Radtke, S. Lazar, G.A. Botton, *Phys. Rev. B* **74** (2006) 115117-1–115117-8.
- [79] F. Morales, F.M.F. de Groot, P. Glatzel, E. Kleimenov, H. Bluhm, M. Hävecker, A. Knop-Gericke, B.M. Weckhuysen *J. Phys. Chem. B* **108** (2004) 16201–16207.
- [80] I. Preda, M. Abbate, A. Gutiérrez, S. Palaćin, A. Vollmer, L. Soriano *J. Elec. Spec. Rel. Phenom.* **156–158** (2007) 111–114.
- [81] P. Graat, M.J. Somers, *Surf. Interface Anal.* **26** (1998) 773–782.
- [82] M.F. López, A. Gutiérrez, F. J. Pérez, M. P. Hierro, F. Pedraza, *Corros. Sci.* **45** (2003) 2043–2053.

- [83] A.A. Galuska, J.C. Uht, N. Marquez, *J. Vac. Sci. Technol. A* 6 (1988) 110–122.
- [84] D. Martinez-Martinez, C. López-Cartés, R. Gago, A. Fernández, J.C. Sánchez-López, *Plasma Process. Polym.* 6 (2009) 462–467.
- [85] NIST XPS database, Version 3.4 (Web Version), National Institute of Standards and Technology, 2006 (<http://srdata.nist.gov/xps/>).
- [86] F.M.F. de Groot, M. Grioni, F. C. Fuggle, J. Ghijsen, G. A. Sawatzky, H. Petersen, *Phys. Rev. B* 40 (1998) 5715–5723.

PUBLICATIONS

CURRICULUM VITAE

First and family name: Rainer Pärna
Date and place of birth: 12.10.1983, Tallinn
Citizenship: Estonian
Marital status: unmarried
Address, telephone, e-mail address: Nõva 15–12, Tartu 50106, Estonia;
+372 53 43 2921; rainer.parna@ut.ee
Current post: University of Tartu, Faculty of Science and Technology,
Institute of Physics; project leader

Education

2007–... University of Tartu, Faculty of Science and Technology,
Material Science, PhD Student
2005–2007 University of Tartu, Faculty of Physics and Chemistry, Master
of Science in Engineering (Chemical Technology of Materials)
2002–2005 University of Tartu, Faculty of Physics and Chemistry,
Bachelor of Science in Engineering (Chemistry of Materials)
1999–2002 Hugo Treffner Gymnasium (special class of biology and
chemistry)

Employment

2011–... University of Tartu, Faculty of Science and Technology,
Institute of Physics; project leader
2007–2011 University of Tartu, Faculty of Science and Technology,
Institute of Physics; engineer
2007–2008 University of Tartu, Faculty of Science and Technology,
graduate school of material science and materials technology;
extraordinary researcher
2006–2007 University of Tartu, Faculty of Physics and Chemistry,
Institute of Physics; engineer
2005–2007 Estonian Nanotechnology Competence Centre; engineer
2004 The Southwestern Company; sales agent

Major research fields

Surface studies of dielectric films (mainly oxides), synchrotron physics, x-ray photoelectron spectroscopy, x-ray absorption spectroscopy and x-ray diffraction.

List of publications

- R. Pärna**, U. Joost, E. Nõmmiste, T. Käämbre, A. Kikas, I. Kuusik, M. Hirsimäki, I. Kink, V. Kisand, Effect of different annealing temperatures and SiO₂/Si(100) substrate on the properties of nickel containing titania thin sol-gel films, *Physica Status Solidi A* (submitted).
- L. Kanninen, N. Jokinen, H. Ali-Lötty, P. Jussila, K. Lahtonen, M. Hirsimäki, M. Valden, M. Kuzmin, **R. Pärna**, E. Nõmmiste, Adsorption structure and bonding of trimesic acid on Cu(100), *Surface Science* 605 (2011) 1968–1978.
- R. Pärna**, U. Joost, E. Nõmmiste, T. Käämbre, A. Kikas, I. Kuusik, M. Hirsimäki, I. Kink, V. Kisand, Effect of cobalt doping and annealing on properties of titania thin films prepared by sol-gel process, *Applied Surface Science* 257 (2011) 6897–6907.
- V. Kisand, U. Joost, V. Reedo, **R. Pärna**, T. Tätte, J. Shulga, A. Saar, L. Matisen, A. Kikas, I. Kink, Investigation of nickel doped sol-gel prepared TiO₂ films, *Applied Surface Science* 256 (2010) 4538–4542.
- R. Pärna**, E. Nõmmiste, A. Kikas, P. Jussila, M. Hirsimäki, M. Valden, V. Kisand, Electron spectroscopic study of passive oxide layer formation on Fe–19Cr–18Ni–1Al–TiC austenitic stainless steel, *Journal of Electron Spectroscopy and Related Phenomena* 182 (2010) 108–114.
- V. Sammelselg, A. Tarre, J. Lu, J. Aarik, A. Niilisk, T. Uustare, I. Netšipailo, R. Rammula, **R. Pärna**, A. Rosental, Structural characterization of TiO₂-Cr₂O₃ nanolaminates by atomic layer deposition, *Surface & Coatings Technology* 204 (2010) 2015–2018.
- A. Tarre, J. Aarik, H. Mändar, A. Niilisk, **R. Pärna**, R. Rammula, T. Uustare, A. Rosental, V. Sammelselg, Atomic layer deposition of Cr₂O₃ thin films: Effect of crystallization on growth and properties, *Applied Surface Science* 254 (2008) 5149–5156.

ELULOOKIRJELDUS

Ees- ja perekonnanimi: Rainer Pärna
Sünniaeg ja koht: 12.10.1983, Tallinn
Kodakondsus: Eesti
Perekonnaseis: vabaabielu
Aadress, telefon, e-post: Nõva 15–12, 50106 Tartu, Eesti; +372 53 43 2921;
rainer.parna@ut.ee
Praegune töökoht, amet: Tartu Ülikool, Loodus- ja tehnoloogiateaduskond,
Füüsika Instituut; projektijuht

Haridus

2007–... Tartu Ülikool, Loodus- ja tehnoloogiateaduskond,
materjaliteadus, doktoratuur
2005–2007 Tartu Ülikool, Füüsika-keemiateaduskond, Tehnikateaduse
magister (keemiline materjalitehnoloogia)
2002–2005 Tartu Ülikool, Füüsika-keemiateaduskond, Tehnikateaduse
bakalaureus (materjalide keemia)
1999–2002 Hugo Treffneri Gümnaasium (bioloogia-keemia eriklass)

Töökogemus

2011–... Tartu Ülikool, Loodus- ja tehnoloogiateaduskond, Füüsika
Instituut; projektijuht
2007–2011 Tartu Ülikool, Loodus- ja tehnoloogiateaduskond, Füüsika
Instituut; insener
2007–2008 Tartu Ülikool, Loodus- ja tehnoloogiateaduskond,
Materjaliteaduse ja materjalide tehnoloogia doktorikool;
erakorraline teadur
2006–2007 Tartu Ülikool, Füüsika-keemiateaduskond, Füüsika Instituut;
insener
2005–2007 Eesti Nanotehnoloogiarenduskeskuse AS; insener
2004 The Southwestern Company; müügiagent

Peamised uurimisvaldkonnad

Dielektriliste kilede (peamiselt oksiidid) pinnauuringud, sünkrotronfüüsika, röntgenfotoelektron-spektroskoopia, röntgenneeldumisspektroskoopia ja röntgen-difraktsioon.

Publikatsioonide loetelu

- R. Pärna**, U. Joost, E. Nõmmiste, T. Käämbre, A. Kikas, I. Kuusik, M. Hirsimäki, I. Kink, V. Kisand, Effect of different annealing temperatures and SiO₂/Si(100) substrate on the properties of nickel containing titania thin sol-gel films, *Physica Status Solidi A* (esitatud avaldamiseks).
- L. Kanninen, N. Jokinen, H. Ali-Lötty, P. Jussila, K. Lahtonen, M. Hirsimäki, M. Valden, M. Kuzmin, **R. Pärna**, E. Nõmmiste, Adsorption structure and bonding of trimesic acid on Cu(100), *Surface Science* 605 (2011) 1968–1978.
- R. Pärna**, U. Joost, E. Nõmmiste, T. Käämbre, A. Kikas, I. Kuusik, M. Hirsimäki, I. Kink, V. Kisand, Effect of cobalt doping and annealing on properties of titania thin films prepared by sol-gel process, *Applied Surface Science* 257 (2011) 6897–6907.
- V. Kisand, U. Joost, V. Reedo, **R. Pärna**, T. Tätte, J. Shulga, A. Saar, L. Matisen, A. Kikas, I. Kink, Investigation of nickel doped sol-gel prepared TiO₂ films, *Applied Surface Science* 256 (2010) 4538–4542.
- R. Pärna**, E. Nõmmiste, A. Kikas, P. Jussila, M. Hirsimäki, M. Valden, V. Kisand, Electron spectroscopic study of passive oxide layer formation on Fe–19Cr–18Ni–1Al–TiC austenitic stainless steel, *Journal of Electron Spectroscopy and Related Phenomena* 182 (2010) 108–114.
- V. Sammelselg, A. Tarre, J. Lu, J. Aarik, A. Niilisk, T. Uustare, I. Netšipailo, R. Rammula, **R. Pärna**, A. Rosental, Structural characterization of TiO₂-Cr₂O₃ nanolaminates by atomic layer deposition, *Surface & Coatings Technology* 204 (2010) 2015–2018.
- A. Tarre, J. Aarik, H. Mändar, A. Niilisk, **R. Pärna**, R. Rammula, T. Uustare, A. Rosental, V. Sammelselg, Atomic layer deposition of Cr₂O₃ thin films: Effect of crystallization on growth and properties, *Applied Surface Science* 254 (2008) 5149–5156.

DISSERTATIONES SCIENTIAE MATERIALIS UNIVERSITATIS TARTUENSIS

1. **Martin Järvekülg.** Tubular microstructures by Hf-, Zr- and Ti-butoxide gel sheet rolling. Tartu, 2011, 112 p.
2. **Sergei Vlassov.** Investigation of nanoscale interactions and mechanical properties of nanostructures using quartz tuning fork based real-time measurements. Tartu, 2011, 171 p.
3. **Margus Kodu.** Pulsed laser deposition of magnesium oxide and barium ternary oxides for plasma display protective layers. Tartu, 2011, 89 p.